Metabolic reprogramming ensures cancer cell survival despite oncogenic signaling blockade

Hui-wen Lue[1], Jennifer Podolak[1], Kevin Kolahi[2], Larry Cheng[3], Soumya Rao[1], Devin Garg[1], Chang-Hui Xue[1], Juha Rantala[1], Jeffrey Tyner[1], Kent Thornburg[2], Ann Martinez-Acevedo[4], Jen-Jane Liu[4], Christopher Amling[4], Charles Truillet[5], Michael Evans[5], Valerie O'Donnell[6], Daniel Nomura[7], Justin Drake[3], Anna Ritz[8], George Thomas[1, 9].

[1]Knight Cancer Institute, Oregon Health and Science University, Portland, Oregon, USA
[2]Knight Cardiovascular Institute, Oregon Health and Science University, Portland, Oregon, USA
[3]Rutgers Cancer Institute of New Jersey, Rutgers, The State University of New Jersey
[4]Dept. of Urology, Oregon Health and Science University, Portland, Oregon, USA
[5]Dept. of Radiology, UCSF School of Medicine
[6]Systems Immunity Research Institute, Cardiff University, Wales
[7]University of California, Berkeley, California, USA
[8]Dept. of Biology, Reed College, Portland, Oregon, USA.
[9]Dept. of Pathology and Laboratory Medicine, Oregon Health and Science University, Portland, Oregon, USA

Abstract

There is limited knowledge about the metabolic reprogramming induced by cancer therapies, and how this contributes to therapeutic resistance. Here we show that although inhibition of PI3K-AKT-mTOR signaling markedly decreased glycolysis and restrained tumor growth, these signaling and metabolic restrictions triggered autophagy, which supplied the metabolites required for the maintenance of mitochondrial respiration and redox homeostasis. Specifically, we found that survival of cancer cells was critically dependent on phospholipase A2 (PLA2) to mobilize lysophospholipids and free fatty acids to sustain fatty acid oxidation and oxidative phosphorylation. Consistent with this, we observed significantly increased lipid droplets, with subsequent mobilization to mitochondria. These changes were abrogated in cells deficient for the essential autophagy gene, *ATG5*. Accordingly, inhibition of PLA2 significantly decreased lipid droplets, decreased oxidative phosphorylation and increased apoptosis. Together, these results describe how treatment-induced autophagy provides nutrients for cancer cell survival and identifies novel co-treatment strategies to override this survival advantage.

Introduction

Despite significant advances in precision cancer therapies, tumor regressions are variable and rarely complete. Although the molecular basis of how cancer cells survive therapies that are designed to kill them (i.e. drug-tolerant "persister" cells) are likely due to a mixed set of mechanisms, we reasoned that at its root are subpopulations of drug-tolerant cancer cells that can rewire their signaling and metabolic networks to adapt to treatment-imposed proliferative, survival and nutrient restrictions. While rewired compensatory oncogenic signaling (e.g. mediated through bypass pathways, receptor amplification, second site mutations) have been well-documented, little is known about the metabolic reprogramming induced by treatment and how this contributes to resistance.

To better understand the metabolic consequences of anti-cancer treatment, we studied metabolic reprogramming in the context of PI3K pathway inhibition. The PI3K pathway which includes the PI3K holoenzyme and its truncal effector kinases AKT and mTOR is essential for cell growth, proliferation, survival and metabolism. Yet, clinical responses to PI3K-AKT-mTOR inhibitors have been modest to date (Fruman and Rommel, 2014; Toska and Baselga, 2016). We hypothesized that the limited ability of PI3K-AKT-mTOR inhibitors to induce cancer cell death was due to the autophagy-mediated metabolic reprogramming that enabled drug-tolerant cells to survive despite therapy-enforced nutrient restrictions. Our hypothesis was based on the knowledge that nutrients derived from autophagic degradation are reutilized to maintain macromolecular synthesis and or oxidized to maintain bioenergetics (Galluzzi et al., 2015). Additionally, due to the central role that the PI3K-AKT-mTOR pathway has in regulating cellular growth, we reasoned that small molecule inhibitors that converge directly or indirectly on this pathway would similarly induce autophagy to sustain drug-tolerant cells, therefore extending the reach of this mechanism of resistance beyond specific PI3K-AKT-mTOR inhibitors.

Thus far, the therapeutic reflex to block autophagy is to add antimalarial lysosomotropic inhibitors such as chloroquine, but the clinical responses to these drugs have been variable and non-curative (Goldberg et al., 2012; Rosenfeld et al., 2014; Shanware et al., 2013; Towers and Thorburn, 2016). Therefore, it would be clinically impactful to directly target the metabolic enzymes mediating autophagy-fueled metabolic processes that drug-tolerant cells are dependent on. However, there has not been any therapeutically tractable metabolic enzymes identified in the setting of therapy-induced autophagy.

Here, we identify CYT387, a JAK inhibitor that induces autophagy by inhibiting mTORC1. Consequently, by relieving the inhibitory signal transmitted from mTORC1 to PI3K, treatment with CYT387 lead to activation of the PI3K-mTORC2/AKT pathway. Combining

CYT387 with MK2206, an allosteric AKT inhibitor did not induce any tumor regressions, despite effectively inhibiting PI3K-AKT-mTORC1/2 activation. Notably, the combination treatment further increased autophagy. This suggested that inhibition of signaling pathways alone would be insufficient to kill all tumor cells. Subsequently, we performed global metabolic profiling to systematically document the immediate metabolic adaptations effected by the therapy-induced autophagic processes. We show that autophagy-mediated metabolic adaptations supported cancer cell survival. Autophagy was required for these metabolic adaptations because these changes were abrogated in cells deficient for the essential autophagy gene, *ATG5*. Subsequently, we identified that PLA2, the rate limiting enzyme responsible for catalyzing the breakdown of phospholipids to lysophospholipids and fatty acids had an important role in the survival of cancer cells. Pharmacological inhibition of this enzyme dampened oxidative phosphorylation, and further increased apoptosis when combined with CYT387-MK2206 combination treatment. Our findings highlight a previously unappreciated role for PLA2 in conferring a survival advantage to drug-tolerant cancer cells in metabolically restricted environments, demonstrate that this enzyme supports autophagy-induced metabolic reprogramming and importantly, provides a path forward for novel co-treatment strategies.

Results

CYT387 induces autophagy through the modulation of the PI3K-AKT-mTOR pathway.

To precisely identify which cancer drugs induce autophagic flux by inhibiting the mTORC1 pathway, we utilized a library of 116 clinically-focused and mechanistically annotated compounds that included activity against two-thirds of the tyrosine kinome as well as other non-tyrosine kinase pathways on a human renal cell carcinoma (RCC) cell line, ACHN (Leonard et al., 2016; Maxson et al., 2016; Maxson et al., 2013) **(Figure S1A: Schematic of workflow; Table S1: list of drugs and known targets).** We monitored mTORC1 activity through phosphorylation of S6, and combined this with a measurement of p62 steady-state levels as an initial screen of autophagy flux (Joachim et al., 2015) in a high-content imaging screen.

Remarkably, the screen identified several structurally different Janus kinase (JAK) inhibitors as potent inducers of autophagic flux, namely, pan-Jak inhibitor (JAK 1, 2, 3), Go6978 (JAK 2), ruxolitinib (Jak 1, 2) and CYT387 (JAK 1, 2). All four drugs potently inhibited S6 phosphorylation, pointing to a mTORC1-dependent mechanism. Since JAK inhibitors as a class of compounds scored highly in our screen, and because CYT387 was the most potent JAK inhibitor to induce autophagic flux and simultaneously decrease S6 phosphorylation in solid tumor cells in our screen, we selected this small molecule for further validation. CYT387

(Momelutinib®) is an orally available JAK 1-2 inhibitor that has improved splenomegaly and reduced anemia in myeloproliferative neoplasia (MPN) patients (Patel et al., 2016; Winton and Kota, 2017). In support of this, CYT387 suppressed the phosphorylation of JAK, its substrate STAT3, and S6 in human RCC and MPN cell lines **(Figure S1B, C**). CYT387 induces autophagy that is reversible, as seen by the reduction in LC3B lipidation within 24hrs of removal of drug, and correlated with reversal of the p-STAT3, p-S6, p-AKT phosphorylation patterns **(Figure S1D)**.

CYT387 treatment of ACHN human RCC cells plated on coverslips resulted in decreased p62 protein expression and phosphorylated–S6 levels by immunofluorescence staining, confirming our high content imaging finding **(Figure 1A)**. Accordingly, we observed that treatment with CYT387 induced autophagy in multiple human RCC and MPN cell lines and was primarily cytostatic **(Figure S1E, F)**. Immunoblots confirmed the induction of autophagy by CYT387 as seen by the conversion of LC3-I to LC3-II, the degradation of p62 and inhibition of mTORC1 (as seen by decrease in phosphorylated-S6) **(Figure 1B)**. We additionally confirmed that CYT387 treatment induced autophagic flux by several different methods*: 1)* we stably expressed a mChery-EGFP-LC3 reported in ACHN cells, which takes advantage of the fact that EGFP fluorescence is quenched in the acidic environment of the autolysosome relative to mCherry (Debnath, 2008). CYT387 treatment resulted in decreased expression of green-yellow cells and increased expression of red cells **(Figure S2A**); *2)* We stained CYT387 treated ACHN cells with the autofluorescent compound monodansylcadaverine (MDC), a marker of autolysosomes and found that CYT387 increased MDC autoflorescence **(Figure S2B**) (Turcotte et al., 2008); *3)* CYT387 increased LC3-II levels in ACHN cells, and this increase was more pronounced in the presence of E64D/pepstatin (which inhibits the protease-induced reconversion of LC3-II into LC3-I), consistent with an increase in autophagosome formation **(Figure S2C)** (Tanida et al., 2005), and *4)* CYT387 increased the number of double-membraned autophagosomes, which are pathognomonic of autophagy as determined by transmission electron microscopy **(Figure S2D**) (Klionsky et al., 2016). Notably, CYT387 was able to induce autophagy in a dose dependent manner in murine embryo fibroblasts (MEFs) that retained the essential autophagy gene, ATG5 (ATG5 +/+), as seen by the lipidation of LC3 **(Figure 1C)** (Cecconi and Levine, 2008; Fung et al., 2008). Conversely, CYT387 did not induce autophagy in ATG5 deficient cells (ATG5 -/-). Likewise, CYT387-induced autophagy was abrogated with siRNA depletion of ATG5 in ACHN cells **(Figure 1D)**. To extend our studies into clinical samples, we exposed patient-derived RCC organotypic cultures to CYT387 treatment for 24 hours. Importantly, CYT387 significantly induced LCB expression while simultaneously reducing

phosphorylated S6 levels **(Figure 1E-F)**. Taken together, these results indicate that CYT387 treatment induces autophagic flux in both human RCC cell lines and patient-derived tumors.

To obtain further insight into the signaling pathways affected by CYT387 treatment, we studied changes in the phosphoproteome of two different human RCC cells (ACHN and SN12C) after CYT387 treatment, using quantitative phosphoproteomics (Moritz et al., 2010; Rush et al., 2005; Zhuang et al., 2013). Supervised hierarchical clustering revealed 513 pST peptides and 180 pY peptides significantly differed between treated and untreated cells (**Figure 1H, Tables S2-9**). We observed two phosphopeptides to be hypophosphorylated at inhibitory residues, T^{1462} and S^{1798} in Tuberous sclerosis complex 2 (TSC2) in CYT387-treated cells (Manning et al., 2002; Roux et al., 2004). Rapamycin-insensitive companion of mTOR (RICTOR) in CYT387-treated cells was hypophosphorylated at T^{1135}. RICTOR is a subunit of mTOR complex 2 (mTORC2) (Kim et al., 2016), but the phosphorylation of T^{1135} is mediated by mTORC1 via induction of p70S6 kinase (Julien et al., 2010) and impedes the ability of mTORC2 to phosphorylate AKT on S^{473} **(Figure 1I)** (Dibble et al., 2009). As expected, ribosomal protein S6 (S6) at residues S^{236} and S^{240}, and STAT3 Y^{705} trended towards hypophosphorylation and p70S6 kinase (RPS6KB) was significantly less active in CYT387-treated cells based on kinase substrate enrichment analyses (KSEA) (**Figure 1J**) (Drake et al., 2012). However, KSEA analyses of AKT motifs were inconclusive as some motifs trended toward increased activity and others trend toward decreased activity in CYT387-treated cells. DAVID analysis of genes corresponding to the phosphopeptides and activated in CYT387-treated cells (**Table S10-11**) also revealed several KEGG pathways that are biologically relevant to CYT387 treatment, including glycolysis, amino acid biosynthesis, and central carbon metabolism (**Figure 1K**) (Huang da et al., 2009a, b). In support of these phosphoproteomics findings, mRNA analysis of CYT387 treated ACHN cells using gene set enrichment (GSEA) of multiple independent datasets revealed significant enrichment of genes involved in several metabolic pathways, while biological modules associated with mTOR (e.g. cell cycle, protein synthesis) were anti-correlated with CYT387 treatment. **(Tables S12-13)**.

Collectively, the phosphoproteome and transcriptome data provides strong evidence that CYT387 treatment reduces mTORC1 signaling to increase TSC2 and mTORC2 signaling leading to AKT activation, and is coupled with changes in metabolic pathways.

PI3K-AKT-mTOR inhibition treatment restrains tumor growth but does not induce tumor regression

We reasoned that the CYT387-induced inhibition of mTORC1 would relieve the inhibitory feedback signal normally transmitted from mTORC1 to PI3K as the phosphoproteomic data suggested via KSEA analysis, and that this would result in hyperactivation of PI3K and AKT, with consequent pro-survival signaling. Consistent with this interpretation, CYT387 treatment caused an increase in AKT T308, the PDK-1 catalyzed site that serves as readout for PI3K signaling in a time-dependent manner **(Figure S3A, B)**. Notably, CYT387 did not dephosphorylate ERK **(Figure S3C)**. Therefore, we sought to identify PI3K-AKT pathway inhibitors that would effectively cooperate with CYT387 to induce apoptosis. We used GDC-0941, a pan-PI3K inhibitor (Sarker et al., 2015); BX795, a PDK-1 inhibitor (Dangelmaier et al., 2014) and MK2206 (Yap et al., 2011), an allosteric AKT inhibitor to chemically deconstruct this signaling pathway, as depicted in the schematic **(Figure S3D-F).** We first assessed the biologic effects of these inhibitors on proliferation and apoptosis in human RCC cells, singly and in combination with CYT387 **(Figure 2A-D)**. While GDC-0941, BX795, MK2206 alone exhibited some anti-proliferative effects, the combination with CYT387 resulted in significantly greater inhibition of proliferation in ACHN and SN12C cells. In marked contrast, all drugs as single agent had little or no effect on apoptosis, but the combination of either agent with CYT387 resulted in increased apoptosis. This was most striking in the CYT387 and MK2206 combination **(Figure 2B, D)**, and therefore we selected MK2206 for further *in vivo* studies. We investigated the mechanisms by which MK2206 and CYT387 cooperated to suppress tumor growth in RCC cells **(Figure 2E-F)**. MK2206 effectively inhibited AKT activation, as documented by dephosphorylation of both p-AKT Thr308 and p-Ser473, and the AKT substrate PRAS40. Consistent with prior results, suppression of AKT induced autophagy as seen by the conversion of LC3-I to LC3-II. Suppression of mTORC1 by CYT387 led to feedback activation of PI3K, as seen by the increase in phosphorylation of p-AKT Thr308 (which serves as a readout for PI3K activity) and mTORC2 (as monitored by AKT Ser473 phosphorylation). Subsequently, combining MK2206 with CYT387 effectively inhibited both AKT and mTORC1 to almost undetectable levels and induced apoptosis (cleaved-caspase3). Thus, by inhibiting the PI3K-AKT-mTOR pathway at proximal and distal nodes, CYT387 and MK2206 combine to shut down PI3K oncogenic signaling However, autophagy still persisted in the combination treatment, pointing to a survival signal that sustains subpopulations of drug-tolerant cancer cells. Notably, the CYT387-MK2206 combination induced autophagy in patient derived organotypic RCC cultures **(Figure 2G)**.

To further define the role of treatment induced-autophagy in mediating survival, we assessed the effects of CYT387 and MK2206 combination treatment on ATG5 -/- and ATG5 +/+ MEFs. The CYT387-MK2206 co-treatment induced more apoptosis in ATG5 -/- MEFS than it did in wild-type controls (demonstrated by increase in cleaved-caspase3) indicating that autophagy protects cells from apoptosis **(Figure 2H)**. Collectively, these results suggest that despite effective inhibition of PI3K-AKT-mTOR signaling with resultant induction of apoptosis, cancer cells are able to simultaneously induce an autophagic-fueled survival pathway.

We next examined the safety and efficacy of CYT387 and MK2206 co-treatment *in vivo* in two xenograft tumor models. While CYT387 or MK2206 alone exhibited anti-tumor effect on ACHN and SN12C xenografts, the combination of CYT387 with MK2206 resulted in significantly greater tumor growth inhibition in ACHN and in SN12C tumor xenografts ($p < 0.001$; Figure, respectively) **(Figure 2I, L)**. Importantly, combination treatment was well tolerated, with no weight loss recorded **(Figure S3G, H)**. Pharmacodynamic studies demonstrated that combination therapy led to the suppression of S6 and AKTS473 phosphorylation **(Figure S3I)**. Consistent with our *in vitro* finding, CYT387 alone had minimal impact on apoptosis. In marked contrast, combination treatment with CYT387 and MK2206 resulted in significant increase in apoptosis **(**established by increase in cleaved-caspase3, $p < 0.001$; **Figure 2J: ACHN xenograft tumors: Figure 2M: SN12C xenograft tumors)** and reduction in proliferation **(**demonstrated by decrease in Ki-67, $p < 0.001$; **Figures 2K: ACHN xenograft tumors: Figure 2N: SN12C xenograft tumors).** However, despite effective inhibition of PI3K-AKT-mTOR signaling, the combination treatment did not induce tumor regression.

Metabolic reprogramming is supported by redox homeostasis

The lack of tumor regression despite effective inhibition of PI3K-AKT-mTOR signaling led us to question whether metabolic reprogramming may sustain the survival of the treated cancer cells. The PI3K-AKT-mTOR pathway regulates multiple steps in glucose uptake and metabolism (Duvel et al., 2010). Therefore, we hypothesized that CYT387 and MK2206 treatment singly, and in combination would negatively impact glucose uptake, aerobic glycolysis and subsequently biosynthetic pathways, resulting in a drug-enforced reduction in glucose availability in the microenvironment. To determine the contribution of CYT387 and MK2206 treatment on the regulation of glycolysis, we measured glucose uptake by ^{18}FDG, lactate excretion and the extracellular acidification rate (ECAR) as readouts for glycolysis. CYT387, MK2206 and the combination significantly decreased glucose uptake and reduced lactate production *in vitro* **(Figure 3A, B)**. The dramatic difference between lactate/glucose ratio in

extracellular media further supports the finding that CYT387 and MK2206 co-treatment inhibits glycolysis *(Control: 1.51; CYT387:0.65; MK2206: 0.81; CYT387+MK2206: 0.37)* This impaired carbon metabolism with treatment also resulted in reduction of cell size **(Figure 3C).** Consistent with the above finding, CYT387 MK2206, and the CYT387-MK2206 combination significantly reduced the ECAR **(Figure 3D, E)**.

Decreased glucose availability with co-treatment might also be reflected in changes with oxidative phosphorylation (OXPHOS) activity, as measured by O2 consumption rate (OCR, an indicator of OXPHOS). However, we found that the OCR/ECAR ratio increased after co-treatment, suggesting a predominant decrease in glycolysis with maintenance of mitochondria-driven OXPHOS **(Figure 3F)**. Consistent with glucose limitation and decreased glycolysis, we observed increased AMPK phosphorylation at Thr-172, an established indicator of metabolic stress **(Figure 3G)**. Importantly, in the setting of glucose deprivation and impairment of the PPP, AMPK has been shown to increase NADPH levels from increased fatty acid oxidation. Specifically, we noted increased levels of NADPH, maintenance of GSSG/GSH ratios and resultant mitigation of reactive oxygen species (ROS) **(Figure 3 H-J)**. These findings are consistent with the role of AMPK in mitigating metabolic stress and promoting cancer cell survival (Jeon et al., 2012). Additionally, AMPK would be predicted to further inhibit mTOR (Gwinn et al., 2008; Inoki et al., 2003). In comparison, we did not see any reduction in PKM2 levels, suggesting that the metabolic switch from aerobic glycolysis to oxidative phosphorylation is not dependent on pyruvate kinase activity (Christofk et al., 2008).

Overall, these findings suggest that CYT387-MK2206 co-treatment by decreasing glucose levels severely reduces the glycolytic capacity needed to supply the bioenergetics needs of the RCC cells. Importantly, this treatment-induced nutrient depleted condition, while suppressing proliferation simultaneously promotes survival by regulating NADPH homeostasis and maintaining mitochondrial-driven oxidation.

PI3K-AKT-mTOR treatment-induced autophagy promotes phospholipid metabolism

Therefore, to comprehensively determine how autophagy contributes to the metabolic needs, we performed global metabolic analysis using liquid chromatography coupled with tandem mass spectrometry (LC-MS/MS) based platform (Louie et al., 2016). These studies revealed that CYT and MK2206, singly and in combination effected changes across multiple pathways **(Figure 4A; Table S14)**. Consistent with the role of the PI3K-AKT-mTOR pathway in the regulation of glycolysis, treatment with these agents was accompanied by reductions in glucose, glucose-6-phosphate, DG3P, PEP, pyruvate and lactate, consistent with the inhibition

of glycolysis **(Figure S4A)**, as described above and also concordant with the gene expression data. Similarly, we also observed reductions in pentose phosphate pathway intermediates, amino acids, TCA cycle intermediates, ribose biosynthesis and corresponding increases purine breakdown products guanine and hypoxanthine **(Figure S4B-E)**. These findings are in keeping with a nutrient-deprived state (i.e. decreased anabolism) with subsequent increased autophagic catabolism to maintain survival (Mizushima et al., 2001). Cells adapt to glucose deprivation by subsisting on fatty acids, mobilized through glycerolipid remodeling, for oxidation and this is consistent with our observation that the most significant metabolite changes were in lipid intermediates including phospholipids, triacylglycerol (TAG), cholesterol esters, diacylglycerol (DAG) and fatty acids (C16:0, C18:0, C18:1) **(Figure 4A, Figure S4F)** (Eaton, 2002; Finn and Dice, 2006; Kerner and Hoppel, 2000).

We further investigated the lipid substrates that were catabolized by autophagy to produce fatty acids for fatty acid oxidation. Steady state metabolite profiling showed significant increases in lysophospholipids and arachidonic acid (C20:4) with corresponding decreases in their phospholipid precursors **(Figure 4B)**. Phospholipids, which include phosphatidylcholine (PC), phosphatidylethanolamine (PE), phosphatidylserine (PS), phosphatidylglycerol (PG) and phosphatidylinositol (PI), are major structural components of cellular membranes. Phospholipase A2 (PLA2) is the enzyme that catalyze the hydrolysis of the phospholipid sn-2 ester bond with subsequent release of lysophospholipids e.g. lysophosphatidylcholine (LPC), alkly-lysophosphatidylcholine (alkyl-LPC), and free fatty acids (Murakami et al., 2011). Accordingly, we found elevated levels of C16:0 LPC, C18:0 LPC, C18:1 LPC, C18-0 alkyl LPC, and corresponding decreases in their phospholipid precursors. Notably, we observed significant decreases in free fatty acids (C16:0, C18:0, C18:1), supporting the idea that phospholipids are hydrolyzed to supply fatty acids for fatty acid oxidation. Consistent with increased arachidonic acid levels in CYT387-MK2206 co-treated cells, we observed increased levels of 14,15-EET, 11,12-EET, 8,9-EET, and 5-HETE pointing to arachidonic acid-P450 mediated generation of eicosanoids **(Figure S5).**

PI3K-AKT-mTOR treatment-induced autophagy facilitates lipid droplet formation and mitochondrial respiration

To protect cells from the destabilizing effects of excess lipids, free fatty acids mobilized by autophagy and destined for oxidation are stored in an intermediate intracellular pool, lipid droplets (LDs) (Thiam et al., 2013). We reasoned that the large changes in glycerolipid redistribution identified by our metabolomics profiling of treated cells would result in increased

number of LDs to support fatty acid oxidation, with subsequent mobilization of fatty acids to mitochondria under these nutrient depleted conditions (Rambold et al., 2015). Consistent with this, we observed that CYT387, MK2206 singly and in combination incrementally and significantly increased the number and size of BODIPY (493/503, green)-labeled LD **(Figure 5A-C)**. Additionally, we incubated ACHN human RCC cells with BODIPY-C12-HPC, a phospholipid containing green fluorescent long-chain fatty acid followed by treatment with vehicle or the CYT387-MK2206 combination. CYT387-MK2206 co-treatment led to a greater degree of incorporation of BODIPY-C12 labeled-fatty acids into lipid droplets relative to vehicle-treated cells. This suggest that CYT387-MK2206 treatment–induced autophagy results in phospholipid hydrolysis that releases fatty acids which are subsequently incorporated into new LDs **(Figure S6)**.

To determine whether the increase in LDs occurred *in vivo*, we stained the vehicle, CYT387, MK2206 and CYT387-MK2206 co-treated xenograft tumors for adipophilin, which belongs to the perilipin family, members of which coat intracellular lipid storage droplets and facilitate metabolic interactions with mitochondria (Sztalryd and Kimmel, 2014). Consistent with the *in vitro* data, the number of adipophilin-positive LDs significantly and incrementally increased with treatment (as measured on treatment day 40 in ACHN xenograft tumors; CYT387<MK2206<CYT387+MK2206; p=0.0046) (**Figure 5D**), indicating that these drug treatments stimulate the formation of lipid droplets *in vivo*. Collectively, this data suggests that the early adaptive and survival changes effected by the initial drug treatment continues to support maintenance of long-term *in vivo* tumor growth.

Next, to further determine if autophagy contributed to LD numbers, we treated ATG5 +/+ and ATG5 -/- MEFs with CYT387, MK2206 and the combination. Autophagy competent ATG5 +/+ MEFs were able to significantly increase LD numbers (**Figure 5E)**. In marked contrast, none of the treatments were able to increase LDs in ATG5 -/- MEFs, confirming that autophagy is required to sustain LD levels **(Figure 5F)**. To investigate the metabolic ramifications of this, we compared oxygen consumption by ATG5 -/- and ATG5 +/+ MEFS when treated with CYT387, MK2206 and the combination. We found that CYT387-MK2206 co-treatment profoundly decreased the ATG5 -/- MEFs mitochondrial OCR and spare respiratory capacity (SRC; this is the quantitative difference between the maximal OCR and the initial basal OCR) indicating that ATG5 -/- MEFs function near their maximal rate and are unable to maintain an adequate level of mitochondrial respiration with CYT387+MK2206 co-treatment due to a deficit in their metabolic

compensatory mechanisms **(Figure 5G, H)**. In contrast, we observed no decrease in mitochondrial OCR and SRC in CYT387-MK2206 co-treated ATG5 +/+ MEFs.

The extent of the metabolic difference between vehicle treated ATG5 -/- to CYT387+MK2206 co-treated MEFs was apparent in the overall ratio of oxidative phosphorylation to aerobic glycolysis (OCR/ECAR), which was 2-fold higher in vehicle-treated than in CYT387-MK2206 co-treated ATG5 -/- MEFs reflective of the need for autophagy to supply the nutrients to maintain mitochondrial OCR under treatment-enforced metabolic restrictions **(Figure 5I)**.

This is in line with a model where autophagy of cellular organelles and membranes during nutrient deprivation produces fatty acids that supply the LD pool, where they are then transferred into mitochondria for β-oxidation. In support of this, we observed that treated RCC cells had significantly increased number of mitochondria **(Figure 5J)**. Accordingly, dual staining of treated ACHN cells with a mitochondrial marker (Mitotracker-orange) and LDs with Bodipy (green) revealed that the LDs were closely associated with the mitochondria, potentially enabling the fatty acids released from lipid droplets to traffic directly from LDs to mitochondria and maximizing the fatty acid oxidation **(Figure 5K)** (Rambold et al., 2015).

Importantly, cancer cells become increasingly dependent on mitochondrial fatty acid oxidation in nutrient-depleted conditions **(Figure 5L)** (Cabodevilla et al., 2013). Consistent with this, using the Mito Fuel Flex Test, we found that human ACHN RCC cells dependence on fatty acid doubled with CYT387-MK2206 co-treatment **(Figure 5M)**. Consequently, oxidation of endogenous fatty acids significantly contributed to the oxidative phosphorylation rate in MK2206+CYT387 co-treated cells compared to control (> 2.5-fold increase, $p<0.0001$) **(Figure 5N).** Consistent with this, induction of fatty acid oxidation by CYT387-MK2206 co-treatment was attenuated in ATG -/- MEFs **(Figure S7)**. In contrast, glutamine supported OCR represented a minority of total OCR in CYT387-MK2206 co-treated ACHN cells **(Figure S8).** Taken together, this suggested that cellular lipid remodeling by the autophagy-lysosome system may supply a considerable fraction of the intracellular lipids-fatty acids irrespective of their external availability.

Inhibiting PLA2 activity decreases autophagy-induced lipid droplets, limits oxidative phosphorylation, and increases apoptosis

Our data implicated hydrolysis of phospholipids as a critical mechanism for the generation of lysophospholipids and fatty acids for fatty acid oxidation in treated RCC cells, and therefore inhibition of this enzymatic activity would negatively impact oxidative phosphorylation and subsequently limit the survival of these cells. To directly test this, we added the PLA2 inhibitor

oleyloxyethylphosphocholine (OOEPC, which inhibits secretory PLA) (Slatter et al., 2016) to CYT387, MK2206 and CYT387-MK2206 co-treated cells and measured LD numbers. Addition of OOEPC significantly reduced the LD abundance in CYT387, MK2206 and CYT387-MK2206 co-treated cells **(Figure 6A, B)**. Since several isoforms of PLA2 exist, we determined their role in reducing LDs. We found that inhibition of calcium-sensitive PLA2 (with cPLA2i) and calcium-insensitive PLA2 (with bromoenol lactone, BEL) were also able to reduce LD number, consistent with the rate-limiting role of PLA2 in mediating phospholipid hydrolysis **(Figure S9)**. To document the kinetics of the new pool of CYT387-MK2206 induced LDs, we performed a time-course experiment to monitor the appearance of LDs following CYT387-MK2206 co-treatment, and ascertained that LDs appeared 2hrs post-treatment and then continuously increased in number during the next 24 hours of monitoring. In contrast, simultaneous addition of OOPEC to the CYT387-MK2206 combination at the start of treatment completely blocked the appearance of LDs. Similarly, addition of OOPEC at 2hrs after co-treatment with CYT387+MK2206 completely inhibited any further increase in LDs. Subsequently, the addition of Etomoxir at 8hrs (which blocks the utilization of fatty acids), resulted in LD accumulation in OOPEC+CYT387+MK2206 treated cells. These results demonstrate that that PLA2 activity is required for LD generation after CYT387-MK2206 co-treatment, and that OOPEC is able to inhibit PLA2 activity **(Figure S10)**.

To directly test the metabolic impact of OOEPC treatment, we first assessed changes in the OCR. We observed a marked decrease in the basal OCR when OOEPC was added to the CYT387-MK2206 combination. Importantly, the addition of OOPEC profoundly reduced the SRC indicating that the inhibition of PLA2 decreases mitochondrial oxidation by reducing fatty acid supply, and impedes the cells' capacity to respond to increased energetic demands **(Figure 6C, D)**. The marked reduction in SRC was similar to our earlier observations in CYT387-MK2206 treated ATG5 -/- MEFs, and is consistent with the model where autophagy-supplied lipid droplets is required to support mitochondrial OCR in metabolically restricted environments **(Figure 5G-I)**. Next, by plotting OCR versus ECAR, we determined the effect of PLA2 inhibition by OOEPC on CYT387-MK2206 treated tumors; this measurement highlighted that untreated ACHN human RCC cells have higher OXPHOS and glycolysis compared to CYT387-MK2206 co-treated cells (**Figure 6E**). The addition of OOEPC markedly decreased OCR in ACHN cells, indicating that these treatments diminished the overall metabolic activity of the cancer cells.

This observed reduction in bioenergetic metabolism led us to determine whether PLA2 inhibition would have an impact on proliferation and apoptosis. Co-treatment with OOEPC had

minimal additional effect on proliferation **(Figure 6F)**. By contrast, the addition of OOEPC significantly increased apoptosis, consistent with its ability to reverse autophagy supplied fatty acids that enable survival **(Figure 6G)**. To further verify that PLA2 inhibition impacted cancer cell survival, we tested a distinct PLA2 inhibitor, varespladib, which has been clinically developed for cardiovascular diseases (Rosenson et al., 2010). Similar to OOEPC, the addition of varespladib to CYT387-MK2206 treated cells decreased LDs and increased apoptosis **(Figure 6H-J)**. Collectively, these data indicate that treatment-induced autophagy provides lysophospholipids and free fatty acids to maintain cancer cell survival despite nutrient depletion.

Discussion

It is now generally accepted that autophagy is cytoprotective in the setting of cancer therapies by enabling cancer cells to mitigate metabolic and therapeutic stresses and thereby ensuring survival (Amaravadi et al., 2011; Rebecca and Amaravadi, 2016; Sehgal et al., 2015). To date, the therapeutic reflex to block autophagy is to add antimalarial lysosomotropic inhibitors such as chloroquine. However, the clinical responses to these have been underwhelming (Goldberg et al., 2012; Rosenfeld et al., 2014; Shanware et al., 2013; Towers and Thorburn, 2016). While the role of autophagy in tumor initiation and progression has been well-documented, little is known about how treatment-induced autophagy mediates cytoprotection and resistance.

Our results demonstrate that cancer cells when acutely exposed to small molecule inhibitors activate the autophagic process to ensure early and lasting metabolic adaptations designed to enhance survival in a nutrient-depleted environment. We first observed the maintenance of oxidative phosphorylation when glucose became limiting due to treatment. Likewise, the coordinate activation of AMPK signaling to ensure protective redox homeostasis to mitigate increased ROS produced by oxidative phosphorylation. Finally, we demonstrated activation of autophagy-mediated membrane glycerophospholipid metabolism with subsequent fatty acid oxidation to generate energy. Accordingly, we find that therapy-induced autophagy purposefully harnesses core biological processes to secure tumor cell fitness and survival. Our experiments involving autophagy-incompetent ATG5 -/- MEFs demonstrate that autophagy is required under conditions of nutrient-depletion to generate lipid droplets and maintain mitochondrial OCR and SRC. It is not coincidental that lipid droplet depletion by pharmacological PLA2 inhibition archived similar results. This is consistent with the model that autophagic digestion of phospholipids, with subsequent hydrolysis within the autolysosome provides LDs with a constant supply of lipids, which can then be trafficked to the mitochondria to

maintain mitochondrial respiration. The subsequent release of these fatty acids from lipid droplets to fuel beta-oxidation, may occur independent of lipophagy as others have observed (Rambold et al., 2015). Additionally, another possible source of fatty acids and amino acids may come from extracellular lysophospholipids and proteins through macropinocytosis.

This study further addresses the wider question of how cancer cells survive despite the inhibition of mTOR, an evolutionary conserved master regulator of cell metabolism, proliferation, growth and survival, and AKT, a committed pro-survival kinase that positively regulates these same processes in both normal and cancer cells (Laplante and Sabatini, 2012; Manning and Cantley, 2007). Undoubtedly, the combination of attenuated proliferation signals, nutrient depletion and metabolic competition for remaining nutrients kills many cells. Accordingly, our data demonstrates that glucose, which is tightly regulated by the PI3K-AKT-mTOR pathway at multiple steps became limiting with treatment, with resultant decrease in glycolysis (Engelman et al., 2006; Hu et al., 2016; Yecies and Manning, 2011). However, the very same conditions that give rise to these nutrient-deprived microenvironments also induced autophagy. Consequently, the autophagic catabolism of membrane phospholipids provides a ready source of free fatty acids that maintains respiration in subpopulations of cancer cells, therefore enabling their survival in a low glucose environment. The increase in fatty acid oxidation and oxidative phosphorylation requires redox homeostasis, and this is provided by the concomitant activation of AMPK, which increases NADPH with subsequent mitigation of ROS. Collectively, treatment-enforced metabolic reprogramming supports cancer cell fitness by providing fatty acids and NADPH to maximize survival.

Since the rate of autophagic release of fatty acids does not match the rate of mitochondrial consumption, these LDs serve a dual purpose: first, as a buffer to reduce lipotoxicity by storing lipid intermediates and second, to transport these lipids to the mitochondria (Rambold et al., 2015; Singh et al., 2009; Unger et al., 2010). Consequently, these energy-strapped residual cancer cells increase fatty acid oxidation, as it is the most energetically efficient way to generate ATP. Long-lived cell types like cardiac myocytes and memory T-cells (Chung et al., 2010; Pearce et al., 2009) depend on fatty acid metabolism for survival, and we see this as yet another example of cancer cells hijacking normal physiological processes to their benefit.

Our screen identified several structurally different Janus-family kinase inhibitors which inhibited mTORC1 and induced autophagic flux. While serendipitous, these findings are not unexpected as small molecules inhibit several kinases and would directly and/or indirectly interdict the PI3K-AKT- mTOR pathway. To date, Janus kinase inhibitors have been approved

for and/or are undergoing late stage clinical trials in MPN, including the focus of this study, CYT387 (Momelutinib®) (Patel et al., 2016; Winton and Kota, 2017). However, complete cytogenetic or molecular responses with JAK inhibitors have not been observed, with clinical benefit mainly resulting from improved performance status due to reduced cytokine levels rather than the elimination of cancer cells (Vannucchi et al., 2015; Verstovsek et al., 2012). Therefore, our finding that JAK inhibitors induce autophagy in both solid tumors and MPN cells which then maintain residual disease potentially through the hydrolysis of phospholipids may offer an explanation as to why this class of inhibitors have not been able to eliminate drug-tolerant cancer cells and effect durable responses.

Combination therapies come with the increased risk of side effects. Notably, CYT387, MK2206 and Varespladib have all been tested in human clinical trials and their maximum tolerated doses have been established and the challenge ahead will be to develop optimal dosing schedules that balances target engagement with side-effects. However, most small molecule inhibitors have favorable toxicity profiles, and metabolic targets would be non-cross resistant and predicted to have a different side effects that are not overlapping. The experience with infectious diseases highlights the importance of combinations to achieve rapid, efficient cancer suppression, i.e. HAART (highly active antiretroviral therapy) in HIV, which is routinely used to produce durable clinical response responses and prevent the emergence of resistance. Polytherapy in cancer is similarly justified and achievable, and here we outline the molecular roadmap for interdicting signaling and metabolism to override treatment-induced autophagy.

Acknowledgements:

We thank Andrew Thorburn, Katherine Ellwood-Yen and Gary Thomas for helpful discussion, Jay Debnath for the *ATG5* +/+ and -/- MEFs, Ernest Frankel for computational advice, Steve Kazmierczak for biochemical analysis**,** Mandy Burns and Ashley Sager for administrative support, Moya Costello and Justin Lallo for artwork, the Histopathology Shared Resource for pathology support, the Massively Parallel Sequencing Shared Resource and Integrated Genomics Shared Resource for genomics support, the Bioanalytical Shared Resource/Pharmacokinetic Core for eicosanoid profiling studies, and the Oregon Translational Research and Development Institute (OTRADI) for high throughput drug screening support.

Grants:

This study was supported by NIH grants R01 CA169172, P30 CA069533 and P30 CA069533 13S5 through OHSU-Knight Cancer Institute, The Hope Foundation (SWOG), OTRADI, WCMC Pilot, and Kure It Cancer Research (GVT). LCC is supported by the National Institute of General Medical Sciences of the National Institutes of Health under award number T32 GM008339. JMD is supported by the Department of Defense Prostate Cancer Research Program W81XWH-15-1-0236, Prostate Cancer Foundation Young Investigator Award, and by a grant from the New Jersey Health Foundation. VOD is an ERC Investigator (LipidArrays) and Royal Society Wolfson Research Merit Award Holder. MJE was supported by the Prostate Cancer Foundation Young Investigator Award, the Department of Defense Prostate Cancer Research Program (W81XWH-15-1-0552), and the National Cancer Institute (R00CA172695, R01CA176671). CT was supported by the Department of Defense Prostate Cancer Research Program (W81XWH-16-1-0435).

Materials and Methods

Cell lines

ACHN, Caki-1, RCC10, SN12C, TK-10, U031, 786-0, UKE-1, SET-2, and HEL were used in this study and were obtained from the ATCC. MEF ATG5 wild type and ATG5-/- were a kind gift from Jay Debnath (UCSF). Cell lines were maintained in Dulbecco's modified Eagle's medium (DMEM) supplemented with 10% fetal bovine serum (FBS) at 37°C in a 5% CO_2 incubator.

Patient tumor *ex vivo* organotypic culture

Tumor tissue samples were collected at the time of surgical removal for consented patients and transported in IMEM +FBS + PS. Tissue was sliced into thin sections using a surgical knife. Sections were cultured on an organotypic insert (EMD#PICMORG50) for 24hours in IMEM+10% FBS+1%PS +50ug/ml holo-transferrin with drug. A section of each tumor was immediately fixed in 10% buffered formalin to confirm tissue viability. After culture, treated tissue sections were fixed in 10% buffered formalin and embedded in paraffin. Paraffin embedded tumors were evaluated for morphology (H&E) and immunofluorescent signaling.

Cell viability and apoptosis analysis

Cell viability assays were performed by plating $3*10^3$ cells/well in 24-well plates in triplicate and treating the following day with the indicated agent. The experiment was continued for 5 days and then the cells were fixed using 4% formaldehyde and stained for 1 hour with Syto60. Fluorescence was measured and quantified and photographs were obtained using a LiCor Odyssey Infrared Imager. The effect of CYT387, MK2206 and the CYT387+MK2206 combination on cell number was assessed as fold of DMSO-treated control cells. Experimental results are the average of at least three independent experiments. Apoptosis was determined using Caspase 3/7-Glo assay kit (Promega) following the manufacturer's instructions. Briefly, 2000 cells per well were plated in 96 well plates and cultured for 72h. Cells were treated with CYT387, MK2206 and the combination of CYT387 and MK2206 for 72h, and then 100 µl reagents were added to each well and incubated for 30 min at room temperature. Caspase 3/7 activity was measured using a luminometer. Luminescence values were normalized by cell numbers. The effect of CYT387, MK2206 and the CYT387+MK2206 combination on caspase 3/7 activation was assessed as fold of DMSO-treated control cells.

High Content Imaging

A 7-point dilution series of 116 small molecule inhibitors covering a 1000x concentration range were plated into three, 384-well plates using the EP Motion automated dispensing system. Control wells with equal volumes of DMSO were included as negative controls. ACHN cells were grown, trypsinized counted, and plated directly into warm drug plates using Multidrop combi dispenser. Plates were incubated for 72hr and subsequently imaged on the Olympus ScanR Platform at 10X magnification performing 4 images per well in 384well plates. Single-cell nuclear and cytoplasmic fluorescent intensities were calculated using the Olympus ScanR Analysis Software: the DAPI-positive region of each cell was used as a boundary to quantitate nuclei counts for analysis of cell growth and integrated nuclear DNA staining intensity was used for cell cycle analysis. A 10-pixel extension of the nuclear region (and not including the nuclear region) was used to quantitate cytoplasmic signal of immunofluorescent staining of p62 protein and phosphorylation of S6. Mean signal intensity of each marker in all cells per well was used as the metric for cytoplasmic marker expression (average intensity of pS6 and p62). Unsupervised hierarchical clustering was used to identify compounds that produced similar pS6 and p62 dose response phenotypes after treatment.

Western Blotting

Cells were plated in 6 well dishes and treated the following day with the indicated agents. Treatments were for 24 hours, after which cells were washed with ice cold PBS and lysed with RIPA buffer (Sigma). Phosphatase inhibitor cocktail set II and protease inhibitor cocktail set III (EMD Millipore) were added at the time of lysis. Lysates were centrifuged at 15,000g x 10 min at 4 degrees C. Protein concentrations were calculated based on a BCA assay (Thermo Scientific) generated standard curve. Proteins were resolved using the NuPAGE Novex Mini Gel system on 4% to 12% Bis-Tris Gels (Invitrogen). For western blotting, equal amounts of cell lysates (15-20 µg of protein) were resolved with SDS-PAGE, and transferred to membranes. The membrane was probed with primary antibodies, washed, and then incubated with corresponding fluorescent secondary antibodies and washed. The fluorescent signal was captured using LI-COR (Lincoln, NE) Odyssey Imaging System, and fluorescent intensity was quantified using the Odyssey software where indicated. The following antibodies were used for Western blots: p-S6 (S240/244), S6, LC3B, p-Akt(S473), p-Akt(T308), Akt, cleaved caspase3 (Cell Signaling Technologies). p-Stat3 (Y705), Stat3 and β-actin (AC15) (Abcam). Ki67 (Dako) and cleaved caspase3 (Cell Signaling Technologies) were used for immunohistochemistry. MK2206 and

CYT387 for *in vitro* and *in vivo* use were purchased from LC Labs and ChemieTek, respectively. BX795 and GDC0941 were purchased from Sigma.

In Vivo Xenograft Studies

6-week old mice were utilized for human renal cell carcinoma xenografts. For both ACHN and SN12C cell lines $2x10^6$ cells were diluted in 50 µl of PBS and 50 µl of Matrigel (BD Biosciences) and were injected subcutaneously into the right and left flank of each mouse.

Tumors were monitored until they reached an average size of 50-80mm3 (approximately 2 weeks), at which point treatments were begun. CYT387 (50mg/kg/day) was administered by oral gavage 5 day/week. MK2206 (60mg/kg/day) were administered by oral gavage 2-3 day/week. CYT387 was dissolved in NMP/Captisol (Cydex) and MK2206 was dissolved in Captisol (Cydex). Tumors and mouse weights were measured twice weekly. At least 6-8 mice per treatment group were included. All mice were euthanized using CO_2 inhalation followed by cervical dislocation per institutional guidelines at Oregon Health and Science University. Experiments were approved by the Institutional Animal Care and Use Committee at OHSU.

Phosphoproteomics screen and data analysis

Enriched phospho-peptides were digested with trypsin and analyzed by mass spectroscopy following the published "Cell Signaling Technology" protocol (Moritz et al., 2010; Rush et al., 2005; Zhuang et al., 2013).

Mass spectrometry data analysis

MS raw files were analyzed via MaxQuant version 1.5.3.30 (Cox and Mann, 2008) and MS/MS fragmentation spectra were searched using Andromeda (Cox et al., 2011) against human canonical and isoform sequences in Swiss-Prot (downloaded in September 2016 from http://uniprot.org) (Apweiler et al., 2004). Quantitative phosphopeptide data were $\log_{10}$ transformed and missing data were imputed before applying quantile normalization as previously described (Drake et al., 2016). Quantitative data can be found in **Supplementary Tables 3-8**. Hierarchical clustering was performed on the Cluster 3.0 program (Eisen et al., 1998), using distance that is based on the Pearson correlation and applying pairwise average linkage analysis. Java Treeview was used to visualize clustering results (Saldanha, 2004).

Kinase substrate enrichment analysis

Kinase substrate enrichment analysis (KSEA) was performed as previously described (Drake et al., 2012). Briefly, the phosphopeptides were rank ordered by fold change, on average, between

CYT387 treatment and control and the enrichment score was calculated using the Kolmogorov-Smirnov statistic. Permutation analysis was conducted to calculate statistical significance. The normalized enrichment score was calculated by dividing the enrichment score by the average of the absolute values of all enrichment scores from the permutation analysis (**Supplementary Tables 9 and 10)**.

DAVID pathway analysis

To generate an appropriate list for use in DAVID (Huang da et al., 2009a, b), phosphopeptides were initially filtered with FDR < 0.20 (**Supplementary Tables 11 and 12**). Phosphopeptides that were 1.5-fold enriched, on average, in either CYT387 treatment or no treatment were selected. Enrichment for a phosphopeptide was reversed if a functional annotation (Hornbeck et al., 2015) indicates protein activity inhibition. To reduce complexity of this list, if multiple phosphopeptides map to a gene, then the most enriched phosphopeptide was selected. The only exception made was if a functional annotation exists for one or more of the phosphopeptides, in which case the most enriched annotated phosphopeptide would be selected. If multiple phosphopeptides mapped to the same gene and had enrichment values that fell into both CYT387 treatment and no treatment, then those phosphopeptides and the corresponding gene were removed from the list to be analyzed. We inputted into DAVID the genes in the CYT387 treatment enriched group (**Supplementary Table 11**) to examine KEGG pathways more active with CYT387 treatment (**Supplementary Table 12**).

Phospho-receptor tyrosine kinase array

The human phospho-receptor tyrosine kinase (phospho-RTK) array kit was purchased from Cell Signaling Technologies, and screened according to the manufacturer's protocol, with 150 µg of protein being used for each experiment. Signal intensity was calculated using LI-COR (Lincoln, NE) Odyssey Imaging System, and fluorescent intensity was quantified using the Odyssey software where indicated.

***In vitro* ^{18}F-FDG uptake assays**

^{18}F-fluorodeoxyglucose was purchased from the radiopharmacy at UCSF. 5 x 10^5 SN12C or ACHN cells were plated an exposed to vehicle or drug for 24 and 48 hours, whereupon the cells were incubated with 0.5 µCi of ^{18}F-FDG for 1 hour at 37° C. The ^{18}F-FDG in the media and the intracellular ^{18}F-FDG was isolated and counted using a gamma counter. The intracellular ^{18}F-

FDG was expressed as a percentage of the total activity added to cells normalized to the cell number.

Metabolomic Profiling of Cancer Cells

Metabolomic data and SRM transitions were performed as previously described (Camarda et al., 2016) and are in **Supplementary Table 13**. Briefly, 2 million cells were plated overnight, serum starved for 2 hours prior to harvesting, after which cells were washed twice with PBS, harvested by scraping, and flash frozen. For nonpolar metabolomic analyses, flash frozen cell pellets were extracted in 4mL of 2:1:1 chloroform/methanol/PBS with internal standards dodecylglycerol (10 nmoles) and pentadecanoic acid (10 nmoles). Organic and aqueous layers were separated by centrifugation, and organic layer was extracted. Aqueous layer was acidified with 0.1% formic acid followed by re-extraction with 2 mL chloroform. The second organic layer was combined with the first extract and dried under nitrogen, after which lipids were resuspended in chloroform (120 µl). A 10 µl aliquot was then analyzed by both single-reaction monitoring (SRM)-based LC-MS/MS or untargeted LC-MS. For polar metabolomic analyses, frozen cell pellets were extracted in 180 µl of 40:40:20 acetonitrile/methanol/water with internal standard d3 N15- serine (1 nmole). Following vortexing and bath sonication, the polar metabolite fraction (supernatant) was isolated by centrifugation. A 20 µl aliquot was then analyzed by both single-reaction monitoring (SRM)-based LC-MS/MS or untargeted LC-MS. For the SRM transitions where we monitor the transition of parent masses to the loss of the headgroup (e.g. loss of phosphocholine from phosphatidylcholine), we have ascertained the acyl chain specificities from previously described procedures (Long et al., 2011). For phospholipids such as PCs and PEs, we ascertained fatty acid acyl chain composition from phospholipids using a mobile phase containing both ammonium hydroxide and formic acid and monitored the fatty acid fragmentations from [M H+HCO2H] m/z at 40 V collision energy in negative ionization mode. For other phospholipids such as PAs and PIs, we monitored the fatty acid fragmentations from [MH] m/z at 40 V collision energy in negative ionization mode in mobile phase containing just ammonium hydroxide. For the lipids that we have measured in this study, the designated acyl chains represent the primary fatty acids that were on the lipid backbone. However, this method is less sensitive than monitoring the loss of headgroup from the phospholipid, and thus we used SRM transitions for many phospholipids where we monitored for loss of headgroups (e.g. PCs, PEs, PSs, PAs, PIs).

Relative levels of metabolites were quantified by integrating the area under the curve for each metabolite, normalizing to internal standard values, and then normalizing to the average values of the control groups (Louie et al., 2016).

Reactive Oxygen Species (ROS) detection

ROS levels were measured with Cellrox Deep Red (Molecular Probes). Cell were plated in a 96 well clear bottom with black sides cell culture plate. After adhering for 24 hours, cells were treated with CYT387 2μM, MK2206 10μM and CYT387 2μM + MK2206 10μM. The complete media +drug was removed after 24hours and replaced with 5μM of Cellrox Deep Red in media. Cells were incubated for 30 min at 37^0C then washed with PBS. Fluorescence signal was detected using a Bioteck Cytation 5 plate reader. Data was analyzed using Prism software.

Cellular respiration

Oxygen consumption and extracellular acidification rates were carried out in a XF96 Seahorse Analyzer (Agilent/Seahorse Bioscience, Billerica, MA, USA). Cells were plated in the wells of 96-well plates (8×10^3 cells/well; XF96 plates, Seahorse Bioscience, North Billerica, MA) and incubated at 37 °C overnight. The next day, cells were treated with indicated drugs for 24 hours and then the medium was changed to XF Assay Medium and loaded with glucose, oligomycin, and 2-DG, respectively, as manufacture's recommendation. Similarly, Mito Fuel Flex Tests were performed on XFe96 Bioanalyzer. At 24 hours post-treatment, all assays were performed following manufacture's protocols.

Immunohistochemistry

Immunostaining was performed following deparaffinization and rehydration of slides. Antigen retrieval was performed in a pressure cooker using citrate buffer (pH 6.0) for 4 min. Nonspecific binding was blocked using Vector mouse IgG blocking serum 30 min at room temperature. Samples were incubated at room temperature with rabbit monoclonal antibodies pS6 (CST #5364) cleaved caspase 3 (Cell Signaling Technologies) (CST#9661), and Ki67 (Dako#M7240). Slides were developed with Vector Immpress rabbit IgG (#MP7401) and Vector Immpress mouse IgG (Vector Laboratories) (#MP7400) for 30 min at room temperature. Chromogenic detection was performed using Vector Immpact DAB (Vector Laboratories) (#SK4105) for 3 min. Slides were counterstained with hematoxylin. A 3DHistech MIDI Scanner (Perkin Elmer) was used to capture whole slide digital images with a 20x objective. Images were converted to into

MRXS files and computer graphic analysis was completed using inForm 1.4.0 Advanced Image Analysis Software (Perkin Elmer).

Morphological and IF evaluation

H&E slides of formalin fixed, paraffin embedded tissue was used to assess morphological integrity of tumor samples. Once integrity was confirmed, immunofluorescent analysis was performed for p-S6 (1:500 CST), p-AKT (1: 200 CST) and LC3B (1:250 CST) (Cell Signaling Technologies). Four micron sections were cut, de-paraffinized and rehydrated. Antigen retrieval was performed using citrate for 4 min in a pressure cooker. Slides were blocked using 2.5% normal goat serum for 30 min then incubated in primary antibody for 1hr followed by secondary antibody mouse anti-rabbit alexa 488 (1:1000, Molecular Probes) for 30 min. Slides were rinsed in PBS, air dried, and coverslipped using Dako mounting media with dapi.

Lipid and mitochondrial staining

Cells were grown on coverslips then treated with drug for 24 hours. Cells were fixed in 4% paraformaldehyde for 15min, rinsed with PBS. Cells were washed with a 1% saponin solution for 15min at room temperature then washed several times in PBS to remove detergent. Cells were then incubated in Bodipy (ThermoFisher #D3922) at a final concentration of 1uM for 10min. Bodipy was removed and slides were rinsed with PBS then air dried and mounted on slides using Dako mounting media with dapi.

To detect mitochondrial levels in treated cells, cells were grown on coverslips for 24 hours. Mitotracker Orange (ThermoFisher # M7511) was diluted in media with drug at a final concentration of 1uM and incubated overnight. Media was removed and cells were fixed with 4% paraformaldehyde for 15 min. Cells were rinsed 2 x 5 min in PBS, incubated in cold acetone at -20C for 10 min. Acetone was removed, cells were washed in PBS, air dried and mounted on slides with Dako mounting media with dapi.

A 3DHistech MIDI Scanner (Perkin Elmer) was used to capture whole slide digital images with a 20x objective. Images were converted to into MRXS files and computer graphic analysis was completed using inForm 1.4.0 Advanced Image Analysis Software (Perkin Elmer).

MDC Staining

Slides were plated on coverslips and allowed to adhere for 24 hours. After adherence, cells were treated with drug for 24 hours. After treatment, drug was removed and cells were washed once in PBS. Cells were labeled with a 50mM concentration of autofluorescent marker

monodansylcadaverine (MDC, Sigma) in PBS for 10 min at 37C. Cells were fixed in 4% formaldehyde for 15 min at room temperature. Cells were washed in PBS 2 x 5 min, and mounted on slides using Dako mounting media with dapi. Coverslips were sealed with clear nail polish and imaged with 3DHistech MIDI Scanner as described above.

Statistical analysis

Mouse tumor size was analyzed by 2-way ANOVA with time and drug as factors, using GraphPad Prism. Mouse weight during treatment was analyzed by repeated measures 2-way ANOVA, with time and drug as factors. A *P* value less than 0.05 was considered statistically significant. Immunohistochemistry: *P*-values were calculated using one-way ANOVA, with Bonferroni's multiple comparison test. * *denotes* $P < 0.05$, ** *denotes* $P < 0.01$, *and* *** *denotes* $P < 0.001$. Metabolite fold-changes were computed and visualized in Python script, using the openpyxl package (for importing Excel files) and the matplotlib package (for visualizing fold changes).

References:

Amaravadi, R.K., Lippincott-Schwartz, J., Yin, X.M., Weiss, W.A., Takebe, N., Timmer, W., DiPaola, R.S., Lotze, M.T., and White, E. (2011). Principles and current strategies for targeting autophagy for cancer treatment. Clin Cancer Res *17*, 654-666.

Apweiler, R., Bairoch, A., Wu, C.H., Barker, W.C., Boeckmann, B., Ferro, S., Gasteiger, E., Huang, H., Lopez, R., Magrane, M.*, et al.* (2004). UniProt: the Universal Protein knowledgebase. Nucleic Acids Res *32*, D115-119.

Cabodevilla, A.G., Sanchez-Caballero, L., Nintou, E., Boiadjieva, V.G., Picatoste, F., Gubern, A., and Claro, E. (2013). Cell survival during complete nutrient deprivation depends on lipid droplet-fueled beta-oxidation of fatty acids. J Biol Chem *288*, 27777-27788.

Camarda, R., Zhou, A.Y., Kohnz, R.A., Balakrishnan, S., Mahieu, C., Anderton, B., Eyob, H., Kajimura, S., Tward, A., Krings, G.*, et al.* (2016). Inhibition of fatty acid oxidation as a therapy for MYC-overexpressing triple-negative breast cancer. Nat Med *22*, 427-432.

Cecconi, F., and Levine, B. (2008). The role of autophagy in mammalian development: cell makeover rather than cell death. Dev Cell *15*, 344-357.

Christofk, H.R., Vander Heiden, M.G., Wu, N., Asara, J.M., and Cantley, L.C. (2008). Pyruvate kinase M2 is a phosphotyrosine-binding protein. Nature *452*, 181-186.

Chung, S., Arrell, D.K., Faustino, R.S., Terzic, A., and Dzeja, P.P. (2010). Glycolytic network restructuring integral to the energetics of embryonic stem cell cardiac differentiation. J Mol Cell Cardiol *48*, 725-734.

Cox, J., and Mann, M. (2008). MaxQuant enables high peptide identification rates, individualized p.p.b.-range mass accuracies and proteome-wide protein quantification. Nat Biotechnol *26*, 1367-1372.

Cox, J., Neuhauser, N., Michalski, A., Scheltema, R.A., Olsen, J.V., and Mann, M. (2011). Andromeda: a peptide search engine integrated into the MaxQuant environment. J Proteome Res *10*, 1794-1805.

Dangelmaier, C., Manne, B.K., Liverani, E., Jin, J., Bray, P., and Kunapuli, S.P. (2014). PDK1 selectively phosphorylates Thr(308) on Akt and contributes to human platelet functional responses. Thromb Haemost *111*, 508-517.

Debnath, J. (2008). Detachment-induced autophagy during anoikis and lumen formation in epithelial acini. Autophagy *4*, 351-353.

Dibble, C.C., Asara, J.M., and Manning, B.D. (2009). Characterization of Rictor phosphorylation sites reveals direct regulation of mTOR complex 2 by S6K1. Mol Cell Biol *29*, 5657-5670.

Drake, J.M., Graham, N.A., Stoyanova, T., Sedghi, A., Goldstein, A.S., Cai, H., Smith, D.A., Zhang, H., Komisopoulou, E., Huang, J.*, et al.* (2012). Oncogene-specific activation of tyrosine kinase networks during prostate cancer progression. Proc Natl Acad Sci U S A *109*, 1643-1648.

Drake, J.M., Paull, E.O., Graham, N.A., Lee, J.K., Smith, B.A., Titz, B., Stoyanova, T., Faltermeier, C.M., Uzunangelov, V., Carlin, D.E.*, et al.* (2016). Phosphoproteome Integration Reveals Patient-Specific Networks in Prostate Cancer. Cell *166*, 1041-1054.

Duvel, K., Yecies, J.L., Menon, S., Raman, P., Lipovsky, A.I., Souza, A.L., Triantafellow, E., Ma, Q., Gorski, R., Cleaver, S.*, et al.* (2010). Activation of a metabolic gene regulatory network downstream of mTOR complex 1. Mol Cell *39*, 171-183.

Eaton, S. (2002). Control of mitochondrial beta-oxidation flux. Prog Lipid Res *41*, 197-239.

Eisen, M.B., Spellman, P.T., Brown, P.O., and Botstein, D. (1998). Cluster analysis and display of genome-wide expression patterns. Proc Natl Acad Sci U S A *95*, 14863-14868.

Engelman, J.A., Luo, J., and Cantley, L.C. (2006). The evolution of phosphatidylinositol 3-kinases as regulators of growth and metabolism. Nat Rev Genet *7*, 606-619.

Finn, P.F., and Dice, J.F. (2006). Proteolytic and lipolytic responses to starvation. Nutrition *22*, 830-844.

Fruman, D.A., and Rommel, C. (2014). PI3K and cancer: lessons, challenges and opportunities. Nat Rev Drug Discov *13*, 140-156.
Fung, C., Lock, R., Gao, S., Salas, E., and Debnath, J. (2008). Induction of autophagy during extracellular matrix detachment promotes cell survival. Mol Biol Cell *19*, 797-806.
Galluzzi, L., Pietrocola, F., Bravo-San Pedro, J.M., Amaravadi, R.K., Baehrecke, E.H., Cecconi, F., Codogno, P., Debnath, J., Gewirtz, D.A., Karantza, V.*, et al.* (2015). Autophagy in malignant transformation and cancer progression. EMBO J *34*, 856-880.
Goldberg, S.B., Supko, J.G., Neal, J.W., Muzikansky, A., Digumarthy, S., Fidias, P., Temel, J.S., Heist, R.S., Shaw, A.T., McCarthy, P.O.*, et al.* (2012). A phase I study of erlotinib and hydroxychloroquine in advanced non-small-cell lung cancer. J Thorac Oncol *7*, 1602-1608.
Gwinn, D.M., Shackelford, D.B., Egan, D.F., Mihaylova, M.M., Mery, A., Vasquez, D.S., Turk, B.E., and Shaw, R.J. (2008). AMPK phosphorylation of raptor mediates a metabolic checkpoint. Mol Cell *30*, 214-226.
Hornbeck, P.V., Zhang, B., Murray, B., Kornhauser, J.M., Latham, V., and Skrzypek, E. (2015). PhosphoSitePlus, 2014: mutations, PTMs and recalibrations. Nucleic Acids Res *43*, D512-520.
Hu, H., Juvekar, A., Lyssiotis, C.A., Lien, E.C., Albeck, J.G., Oh, D., Varma, G., Hung, Y.P., Ullas, S., Lauring, J.*, et al.* (2016). Phosphoinositide 3-Kinase Regulates Glycolysis through Mobilization of Aldolase from the Actin Cytoskeleton. Cell *164*, 433-446.
Huang da, W., Sherman, B.T., and Lempicki, R.A. (2009a). Bioinformatics enrichment tools: paths toward the comprehensive functional analysis of large gene lists. Nucleic Acids Res *37*, 1-13.
Huang da, W., Sherman, B.T., and Lempicki, R.A. (2009b). Systematic and integrative analysis of large gene lists using DAVID bioinformatics resources. Nat Protoc *4*, 44-57.
Inoki, K., Zhu, T., and Guan, K.L. (2003). TSC2 mediates cellular energy response to control cell growth and survival. Cell *115*, 577-590.
Jeon, S.M., Chandel, N.S., and Hay, N. (2012). AMPK regulates NADPH homeostasis to promote tumour cell survival during energy stress. Nature *485*, 661-665.
Joachim, J., Jiang, M., McKnight, N.C., Howell, M., and Tooze, S.A. (2015). High-throughput screening approaches to identify regulators of mammalian autophagy. Methods *75*, 96-104.
Julien, L.A., Carriere, A., Moreau, J., and Roux, P.P. (2010). mTORC1-activated S6K1 phosphorylates Rictor on threonine 1135 and regulates mTORC2 signaling. Mol Cell Biol *30*, 908-921.
Kerner, J., and Hoppel, C. (2000). Fatty acid import into mitochondria. Biochim Biophys Acta *1486*, 1-17.
Kim, L.C., Cook, R.S., and Chen, J. (2016). mTORC1 and mTORC2 in cancer and the tumor microenvironment. Oncogene.
Klionsky, D.J., Abdelmohsen, K., Abe, A., Abedin, M.J., Abeliovich, H., Acevedo Arozena, A., Adachi, H., Adams, C.M., Adams, P.D., Adeli, K.*, et al.* (2016). Guidelines for the use and interpretation of assays for monitoring autophagy (3rd edition). Autophagy *12*, 1-222.
Laplante, M., and Sabatini, D.M. (2012). mTOR signaling in growth control and disease. Cell *149*, 274-293.
Leonard, J.T., Rowley, J.S., Eide, C.A., Traer, E., Hayes-Lattin, B., Loriaux, M., Spurgeon, S.E., Druker, B.J., Tyner, J.W., and Chang, B.H. (2016). Targeting BCL-2 and ABL/LYN in Philadelphia chromosome-positive acute lymphoblastic leukemia. Sci Transl Med *8*, 354ra114.
Long, J.Z., Cisar, J.S., Milliken, D., Niessen, S., Wang, C., Trauger, S.A., Siuzdak, G., and Cravatt, B.F. (2011). Metabolomics annotates ABHD3 as a physiologic regulator of medium-chain phospholipids. Nat Chem Biol *7*, 763-765.
Louie, S.M., Grossman, E.A., Crawford, L.A., Ding, L., Camarda, R., Huffman, T.R., Miyamoto, D.K., Goga, A., Weerapana, E., and Nomura, D.K. (2016). GSTP1 Is a Driver of Triple-Negative Breast Cancer Cell Metabolism and Pathogenicity. Cell Chem Biol *23*, 567-578.

Manning, B.D., and Cantley, L.C. (2007). AKT/PKB signaling: navigating downstream. Cell *129*, 1261-1274.
Manning, B.D., Tee, A.R., Logsdon, M.N., Blenis, J., and Cantley, L.C. (2002). Identification of the tuberous sclerosis complex-2 tumor suppressor gene product tuberin as a target of the phosphoinositide 3-kinase/akt pathway. Mol Cell *10*, 151-162.
Maxson, J.E., Abel, M.L., Wang, J., Deng, X., Reckel, S., Luty, S.B., Sun, H., Gorenstein, J., Hughes, S.B., Bottomly, D.*, et al.* (2016). Identification and Characterization of Tyrosine Kinase Nonreceptor 2 Mutations in Leukemia through Integration of Kinase Inhibitor Screening and Genomic Analysis. Cancer Res *76*, 127-138.
Maxson, J.E., Gotlib, J., Pollyea, D.A., Fleischman, A.G., Agarwal, A., Eide, C.A., Bottomly, D., Wilmot, B., McWeeney, S.K., Tognon, C.E.*, et al.* (2013). Oncogenic CSF3R mutations in chronic neutrophilic leukemia and atypical CML. N Engl J Med *368*, 1781-1790.
Mizushima, N., Yamamoto, A., Hatano, M., Kobayashi, Y., Kabeya, Y., Suzuki, K., Tokuhisa, T., Ohsumi, Y., and Yoshimori, T. (2001). Dissection of autophagosome formation using Apg5-deficient mouse embryonic stem cells. J Cell Biol *152*, 657-668.
Moritz, A., Li, Y., Guo, A., Villen, J., Wang, Y., MacNeill, J., Kornhauser, J., Sprott, K., Zhou, J., Possemato, A.*, et al.* (2010). Akt-RSK-S6 kinase signaling networks activated by oncogenic receptor tyrosine kinases. Sci Signal *3*, ra64.
Murakami, M., Taketomi, Y., Miki, Y., Sato, H., Hirabayashi, T., and Yamamoto, K. (2011). Recent progress in phospholipase A(2) research: from cells to animals to humans. Prog Lipid Res *50*, 152-192.
Patel, A.B., Vellore, N.A., and Deininger, M.W. (2016). New Strategies in Myeloproliferative Neoplasms: The Evolving Genetic and Therapeutic Landscape. Clin Cancer Res *22*, 1037-1047.
Pearce, E.L., Walsh, M.C., Cejas, P.J., Harms, G.M., Shen, H., Wang, L.S., Jones, R.G., and Choi, Y. (2009). Enhancing CD8 T-cell memory by modulating fatty acid metabolism. Nature *460*, 103-107.
Rambold, A.S., Cohen, S., and Lippincott-Schwartz, J. (2015). Fatty acid trafficking in starved cells: regulation by lipid droplet lipolysis, autophagy, and mitochondrial fusion dynamics. Dev Cell *32*, 678-692.
Rebecca, V.W., and Amaravadi, R.K. (2016). Emerging strategies to effectively target autophagy in cancer. Oncogene *35*, 1-11.
Rosenfeld, M.R., Ye, X., Supko, J.G., Desideri, S., Grossman, S.A., Brem, S., Mikkelson, T., Wang, D., Chang, Y.C., Hu, J.*, et al.* (2014). A phase I/II trial of hydroxychloroquine in conjunction with radiation therapy and concurrent and adjuvant temozolomide in patients with newly diagnosed glioblastoma multiforme. Autophagy *10*, 1359-1368.
Rosenson, R.S., Hislop, C., Elliott, M., Stasiv, Y., Goulder, M., and Waters, D. (2010). Effects of varespladib methyl on biomarkers and major cardiovascular events in acute coronary syndrome patients. J Am Coll Cardiol *56*, 1079-1088.
Roux, P.P., Ballif, B.A., Anjum, R., Gygi, S.P., and Blenis, J. (2004). Tumor-promoting phorbol esters and activated Ras inactivate the tuberous sclerosis tumor suppressor complex via p90 ribosomal S6 kinase. Proc Natl Acad Sci U S A *101*, 13489-13494.
Rush, J., Moritz, A., Lee, K.A., Guo, A., Goss, V.L., Spek, E.J., Zhang, H., Zha, X.M., Polakiewicz, R.D., and Comb, M.J. (2005). Immunoaffinity profiling of tyrosine phosphorylation in cancer cells. Nat Biotechnol *23*, 94-101.
Saldanha, A.J. (2004). Java Treeview--extensible visualization of microarray data. Bioinformatics *20*, 3246-3248.
Sarker, D., Ang, J.E., Baird, R., Kristeleit, R., Shah, K., Moreno, V., Clarke, P.A., Raynaud, F.I., Levy, G., Ware, J.A.*, et al.* (2015). First-in-human phase I study of pictilisib (GDC-0941), a potent pan-class I phosphatidylinositol-3-kinase (PI3K) inhibitor, in patients with advanced solid tumors. Clin Cancer Res *21*, 77-86.

Sehgal, A.R., Konig, H., Johnson, D.E., Tang, D., Amaravadi, R.K., Boyiadzis, M., and Lotze, M.T. (2015). You eat what you are: autophagy inhibition as a therapeutic strategy in leukemia. Leukemia *29*, 517-525.
Shanware, N.P., Bray, K., and Abraham, R.T. (2013). The PI3K, metabolic, and autophagy networks: interactive partners in cellular health and disease. Annu Rev Pharmacol Toxicol *53*, 89-106.
Singh, R., Kaushik, S., Wang, Y., Xiang, Y., Novak, I., Komatsu, M., Tanaka, K., Cuervo, A.M., and Czaja, M.J. (2009). Autophagy regulates lipid metabolism. Nature *458*, 1131-1135.
Slatter, D.A., Aldrovandi, M., O'Connor, A., Allen, S.M., Brasher, C.J., Murphy, R.C., Mecklemann, S., Ravi, S., Darley-Usmar, V., and O'Donnell, V.B. (2016). Mapping the Human Platelet Lipidome Reveals Cytosolic Phospholipase A2 as a Regulator of Mitochondrial Bioenergetics during Activation. Cell Metab *23*, 930-944.
Sztalryd, C., and Kimmel, A.R. (2014). Perilipins: lipid droplet coat proteins adapted for tissue-specific energy storage and utilization, and lipid cytoprotection. Biochimie *96*, 96-101.
Tanida, I., Minematsu-Ikeguchi, N., Ueno, T., and Kominami, E. (2005). Lysosomal turnover, but not a cellular level, of endogenous LC3 is a marker for autophagy. Autophagy *1*, 84-91.
Thiam, A.R., Farese, R.V., Jr., and Walther, T.C. (2013). The biophysics and cell biology of lipid droplets. Nat Rev Mol Cell Biol *14*, 775-786.
Toska, E., and Baselga, J. (2016). Pharmacology in the Era of Targeted Therapies: The Case of PI3K Inhibitors. Clin Cancer Res *22*, 2099-2101.
Towers, C.G., and Thorburn, A. (2016). Therapeutic Targeting of Autophagy. EBioMedicine *14*, 15-23.
Turcotte, S., Chan, D.A., Sutphin, P.D., Hay, M.P., Denny, W.A., and Giaccia, A.J. (2008). A molecule targeting VHL-deficient renal cell carcinoma that induces autophagy. Cancer Cell *14*, 90-102.
Unger, R.H., Clark, G.O., Scherer, P.E., and Orci, L. (2010). Lipid homeostasis, lipotoxicity and the metabolic syndrome. Biochim Biophys Acta *1801*, 209-214.
Vannucchi, A.M., Kiladjian, J.J., Griesshammer, M., Masszi, T., Durrant, S., Passamonti, F., Harrison, C.N., Pane, F., Zachee, P., Mesa, R.*, et al.* (2015). Ruxolitinib versus standard therapy for the treatment of polycythemia vera. N Engl J Med *372*, 426-435.
Verstovsek, S., Mesa, R.A., Gotlib, J., Levy, R.S., Gupta, V., DiPersio, J.F., Catalano, J.V., Deininger, M., Miller, C., Silver, R.T.*, et al.* (2012). A double-blind, placebo-controlled trial of ruxolitinib for myelofibrosis. N Engl J Med *366*, 799-807.
Winton, E.F., and Kota, V. (2017). Momelotinib in myelofibrosis: JAK1/2 inhibitor with a role in treating and understanding the anemia. Future Oncol *13*, 395-407.
Yap, T.A., Yan, L., Patnaik, A., Fearen, I., Olmos, D., Papadopoulos, K., Baird, R.D., Delgado, L., Taylor, A., Lupinacci, L.*, et al.* (2011). First-in-man clinical trial of the oral pan-AKT inhibitor MK-2206 in patients with advanced solid tumors. J Clin Oncol *29*, 4688-4695.
Yecies, J.L., and Manning, B.D. (2011). Transcriptional control of cellular metabolism by mTOR signaling. Cancer Res *71*, 2815-2820.
Zhuang, G., Yu, K., Jiang, Z., Chung, A., Yao, J., Ha, C., Toy, K., Soriano, R., Haley, B., Blackwood, E.*, et al.* (2013). Phosphoproteomic analysis implicates the mTORC2-FoxO1 axis in VEGF signaling and feedback activation of receptor tyrosine kinases. Sci Signal *6*, ra25.

Figure legends

Figure 1. CYT387 induces autophagy in human cancer cell lines and patient-derived models

(A) ACHN cells were grown on coverslips, treated with CYT387 for 24hr and stained p62 and p-S6.

(B) ACHN cells were treated with increasing doses of CYT387 (0-2μM) and immunoblotted with LC3, p62, p-S6, total S6, p-STAT3, total STAT3 and β-actin.

(C) *ATG5*$^{+/+}$ and *ATG5*$^{-/-}$ murine embryonic fibroblasts (MEFs) were treated with 0-3μM CYT387 for 24 hr and LC3 processing was evaluated by immunoblotting.

(D) Immunoblot for LC3 and p-STAT3 and ATG5 in ACHN cells transiently transfected with siRNA against *ATG5*. β-actin was used for loading control.

(E) Patient derived organotypic cultures treated with CYT387 for 24hr and stained with p-S6 and LC3B (images from two different patient tumors shown)

(F, G) Quantification of **(F)** p-S6 and, **(G)** LC3B staining in patient derived organotypic cultures, quantified (bar graph; n=10 patients)

(H) Supervised hierarchical clustering heatmaps of phosphoserine and phosphothreonine peptides (pST) and phosphotyrosine peptides (pY) identified from CYT387 treated and untreated ACHN and SN12C human RCC cells with two technical replicates. 513 unique pST phosphopeptides (rows) and 180 unique pY phosphopeptides were either 4-fold more enriched or 4-fold less enriched, on average (t-test $p<0.2$), in CYT387-treated cells compared to untreated cells. (Phosphopeptide lists are in **Tables S2 and S3**)

(I) Relative phosphorylation abundance between ACHN and SN12C CYT387-treated and -untreated cells. RPS6 S^{236}, S^{240} was found in the pST unsupervised heatmap. Ctrl = Control; CYT = CYT387. Unpaired t-test: * $p<0.05$; ** $p<0.01$; *** $p<0.001$

(J) Kinase-substrate enrichment analysis (KSEA) of CYT387-treated and untreated pST data (Hits $\geq$ 5; FDR <0.05). Positive NKS (Normalized Kolmogorov-Smirnov Score) infer greater kinase activity in CYT387-treated cells while negative NKS indicate greater activity in untreated cells (Unfiltered summary is in **Table S4**)

(K) KEGG pathways found from DAVID analysis of relatively active genes due to CYT387 treatment. DAVID input list was generated from interpreting functional annotations of pSTY data. (Complete pathway list is in **Table S2**)

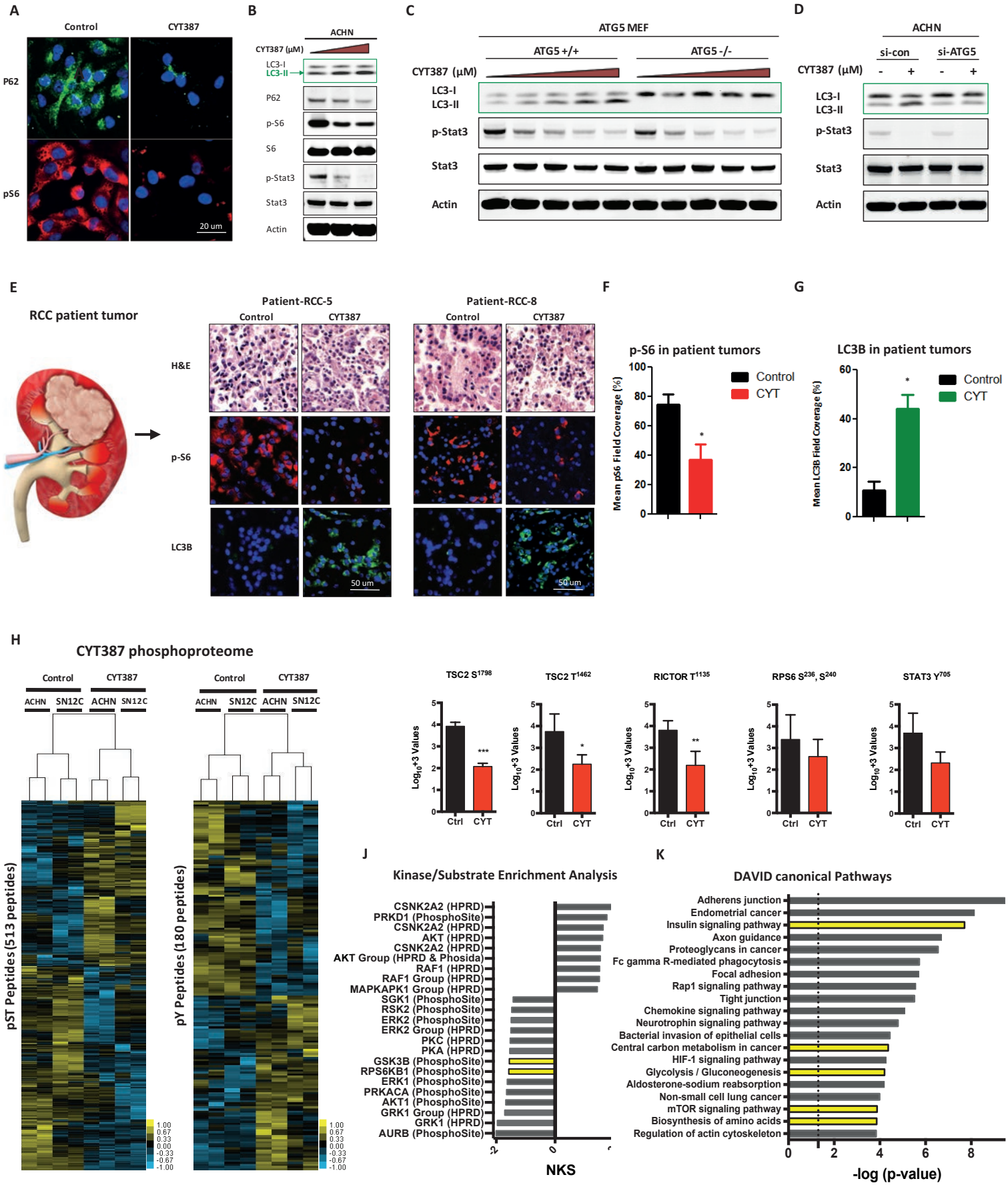
A
Control
CYT387
P62
pS6
20 um
B
ACHN
CYT387 (μM)
LC3-I
LC3-II
P62
p-S6
S6
p-Stat3
Stat3
Actin
C
ATG5 MEF
ATG5 +/+
ATG5 -/-
CYT387 (μM)
LC3-I
LC3-II
p-Stat3
Stat3
Actin
D
ACHN
si-con
si-ATG5
CYT387 (μM)
- + - +
LC3-I
LC3-II
p-Stat3
Stat3
Actin
E
RCC patient tumor
Patient-RCC-5
Patient-RCC-8
Control
CYT387
H&E
p-S6
LC3B
50 um
F
p-S6 in patient tumors
Mean p56 Field Coverage (%)
Control
CYT
G
LC3B in patient tumors
Mean LC3B Field Coverage (%)
Control
CYT
H
CYT387 phosphoproteome
Control
CYT387
ACHN
SN12C
pST Peptides (513 peptides)
pY Peptides (180 peptides)
TSC2 S1798
TSC2 T1462
RICTOR T1135
RPS6 S236, S240
STAT3 Y705
Log10+3 Values
Ctrl
CYT
J
Kinase/Substrate Enrichment Analysis
CSNK2A2 (HPRD)
PRKD1 (PhosphoSite)
CSNK2A2 (HPRD)
AKT (HPRD)
CSNK2A2 (HPRD)
AKT Group (HPRD & Phosida)
RAF1 (HPRD)
RAF1 Group (HPRD)
MAPKAPK1 Group (HPRD)
SGK1 (PhosphoSite)
RSK2 (PhosphoSite)
ERK2 (PhosphoSite)
ERK2 Group (HPRD)
PKC (HPRD)
PKA (HPRD)
GSK3B (PhosphoSite)
RPS6KB1 (PhosphoSite)
ERK1 (PhosphoSite)
PRKACA (PhosphoSite)
AKT1 (PhosphoSite)
GRK1 Group (HPRD)
GRK1 (HPRD)
AURB (PhosphoSite)
NKS
K
DAVID canonical Pathways
Adherens junction
Endometrial cancer
Insulin signaling pathway
Axon guidance
Proteoglycans in cancer
Fc gamma R-mediated phagocytosis
Focal adhesion
Rap1 signaling pathway
Tight junction
Chemokine signaling pathway
Neurotrophin signaling pathway
Bacterial invasion of epithelial cells
Central carbon metabolism in cancer
HIF-1 signaling pathway
Glycolysis / Gluconeogenesis
Aldosterone-sodium reabsorption
Non-small cell lung cancer
mTOR signaling pathway
Biosynthesis of amino acids
Regulation of actin cytoskeleton
-log (p-value)

Figure S1. High content imaging to identify small molecule inhibitors that induce autophagy, Related to Figure 1

(A) Schematic of high content imaging screen that measures p62 and p-S6, with magnification of lead small molecule inhibitors that decrease the expression of both proteins (list of drugs and targets is in **Table S1**).

(B) CYT387 inhibits JAK signaling in a dose-dependent manner in multiple human RCC cell lines. Immunoblots for p-JAK, total JAK, p-STAT3 and total STAT3. β-actin was used for loading control.

(C) CYT387 induces autophagy in multiple human MPN and RCC cells. LC3 processing and p-S6 evaluated by western blot following 24 hr of drug treatment.

(D) CYT387 induces reversible autophagy. ACHN cells were grown in the absence (control) or presence of 2 μM CYT387 for 24hr, followed by withdrawal of CYT387 for 24hr, lysed, and probed with antibodies to LC3, p-STAT3, total STAT3, p-S6, total S6, P-Akt Ser 473, and total AKT. β-actin as loading control.

(E) CYT 387 reduces proliferation in most human RCC and MPN cells lines.
Pharmacological action of CYT387 in multiple human RCC cell lines, with induction of autophagy, as documented by LC3 immunoblots.

(F) Single agent CYT 387 treatment in most RCC cells lines demonstrates minimal effect on apoptosis. Bar graphs shows caspase 3/7 activation (apoptosis).

A

Schematic of high content imaging screen for autophagy flux inducers

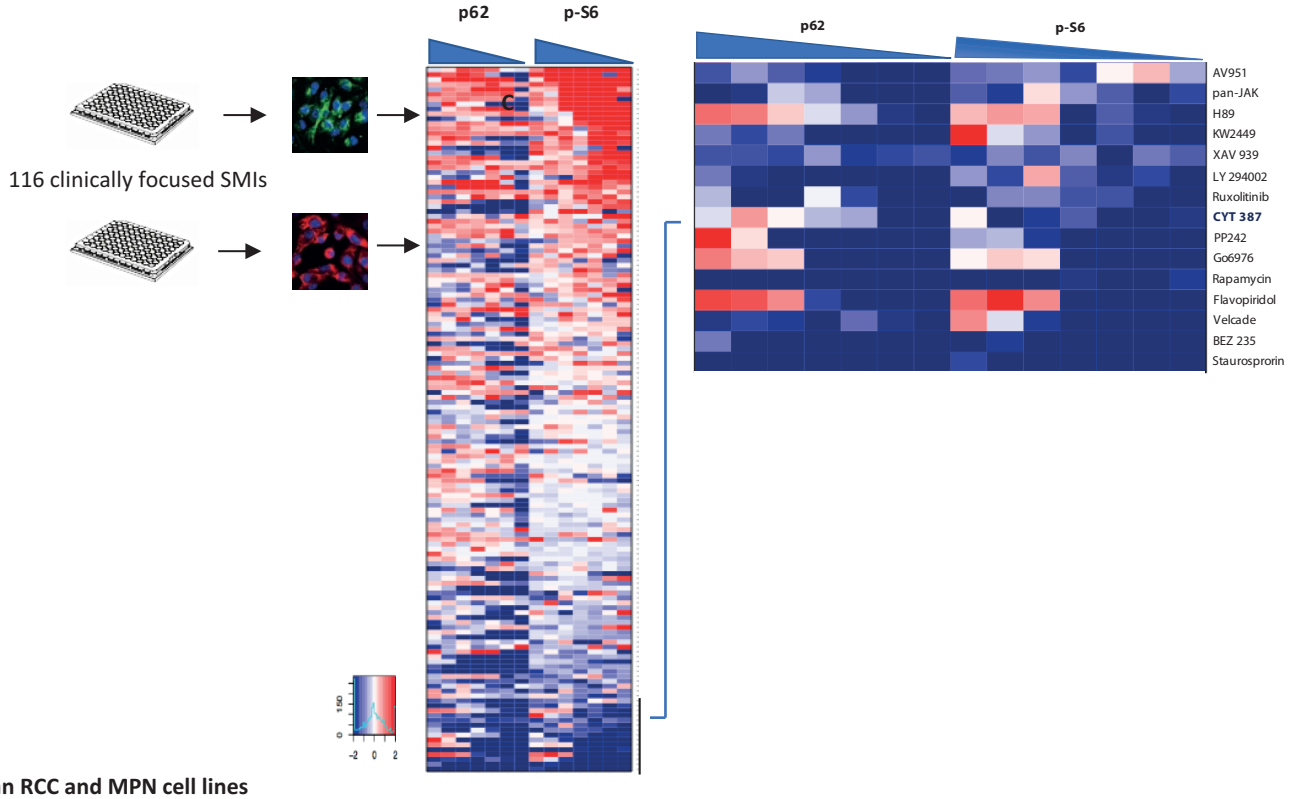

B

Human RCC and MPN cell lines

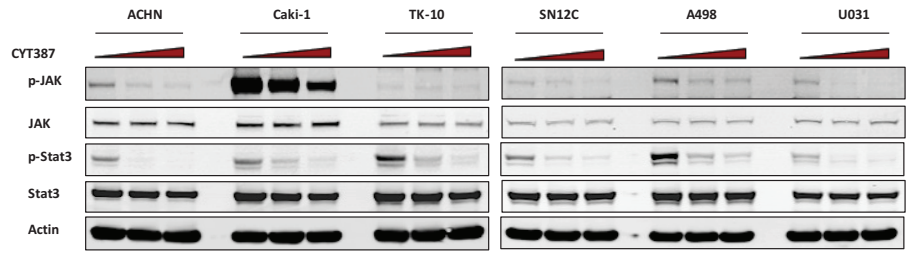

C

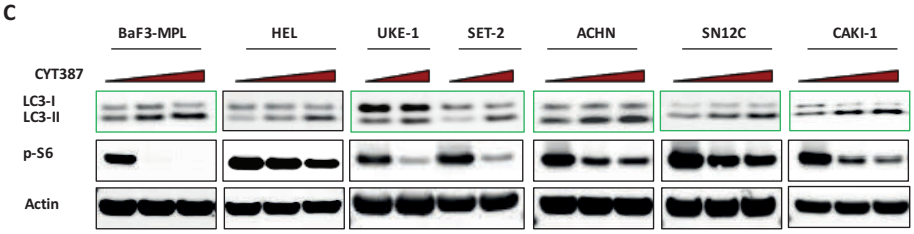

D

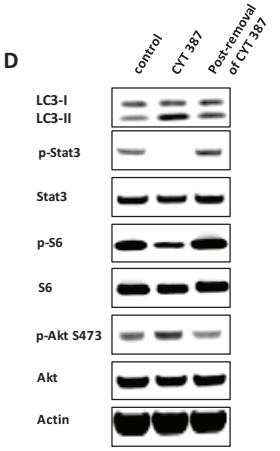

E

Human RCC and MPN cell lines: Viability

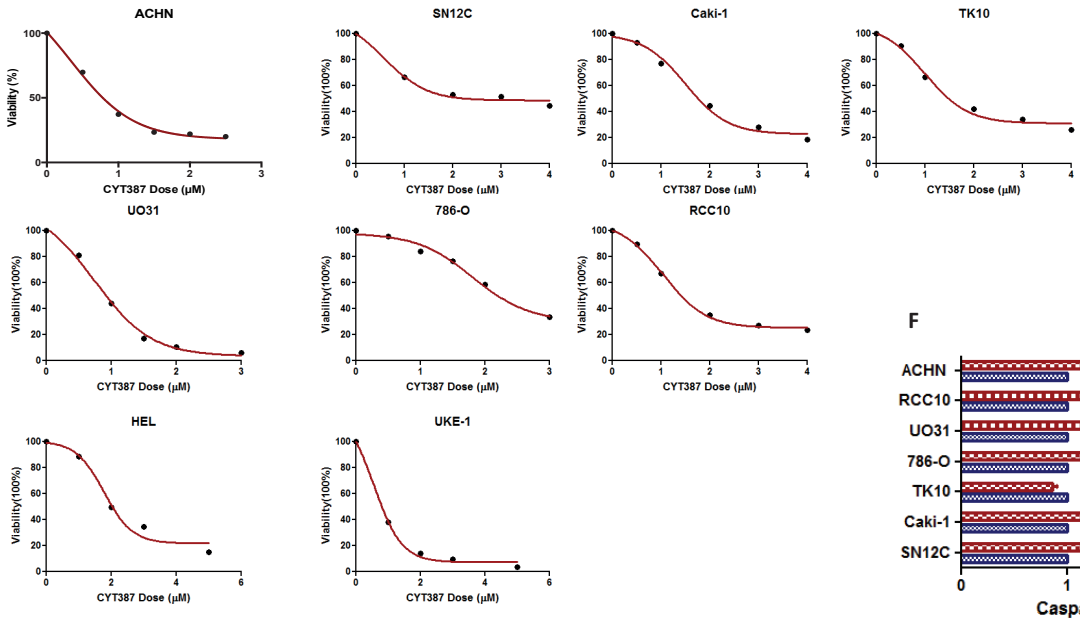

F

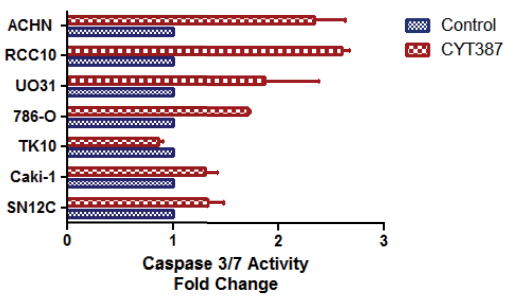

Figure S2. Validation of CYT387 as an inducer of autophagic flux, Related to Figure 1.

(A) ACHN cells stably expressing mCherry-GFP were treated with 2μM of CYT387 to document autophagic flux: yellow to red. Insert: high power. GFP-mCherry ratio measured by image analysis.

(B) Autophagic vacuoles stained with green with monodansylcadaverine (MDC). ACHN cells were treated with CYT387, in the presence or absence or absence of E64D and pepstatin. Cells were fixed, washed with PBS and observed directly under microscope and representative images are shown. The increase in MDC staining is quantified (bar graph; * $p<0.001$)

(C) Expression of LC3 (LC3-I and LC3-II) determined by immunoblotting in cell extracts from ACHN cells exposed to 2μM CYT387 for 24 hr in the presence or absence of E64d and pepstatin.

(D) Transmission Electron Microscopy (TEM) micrographs of CYT387-treated ACHN cells show increase in autophagosome, autolysosomes, lipid droplets and mitochondria (data represents >3 experiments).

Figure panels:
Left: Control: Low mag (1900x) + High mag (6800x) insert
Middle: CYT387 treated: Low mag (1900x) + High mag (6800x) insert
Green arrows: Autolysosome
Red Arrows: Autophagosome
Blue Arrows: Lipid Droplets
M: Mitochondria
Right: Pseudocolor of CYT387 treated (High mag insert from middle panel):
Deep Blue: Mitochondria
Red: Autolysosome
Orange: Autophagosome
Bright Blue: Lipid Droplet

A

GFP-mCherry-LC3 reporter

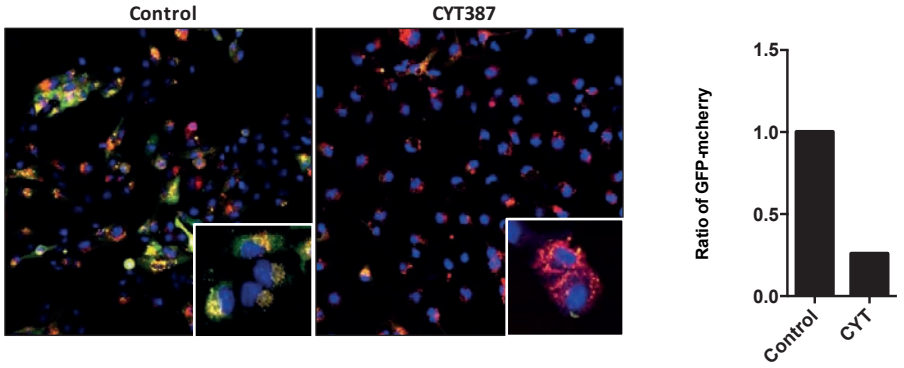

B

MDC autolysome tracking

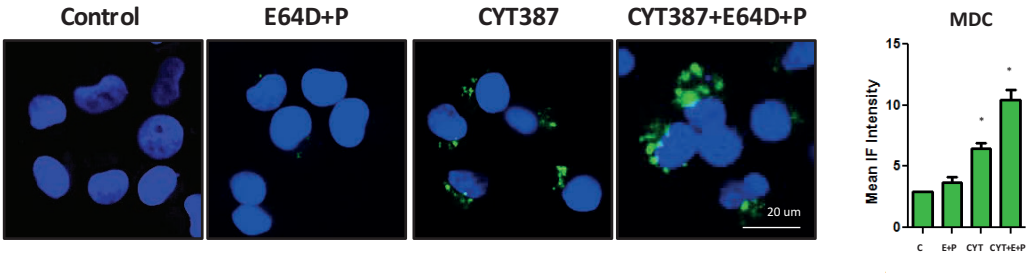

C

E64D/Pepstatin

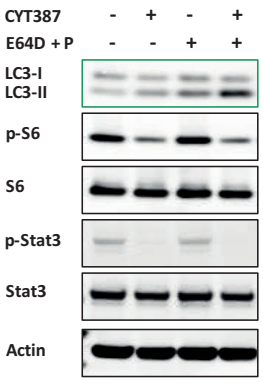

D

Transmission Electron Microscopy

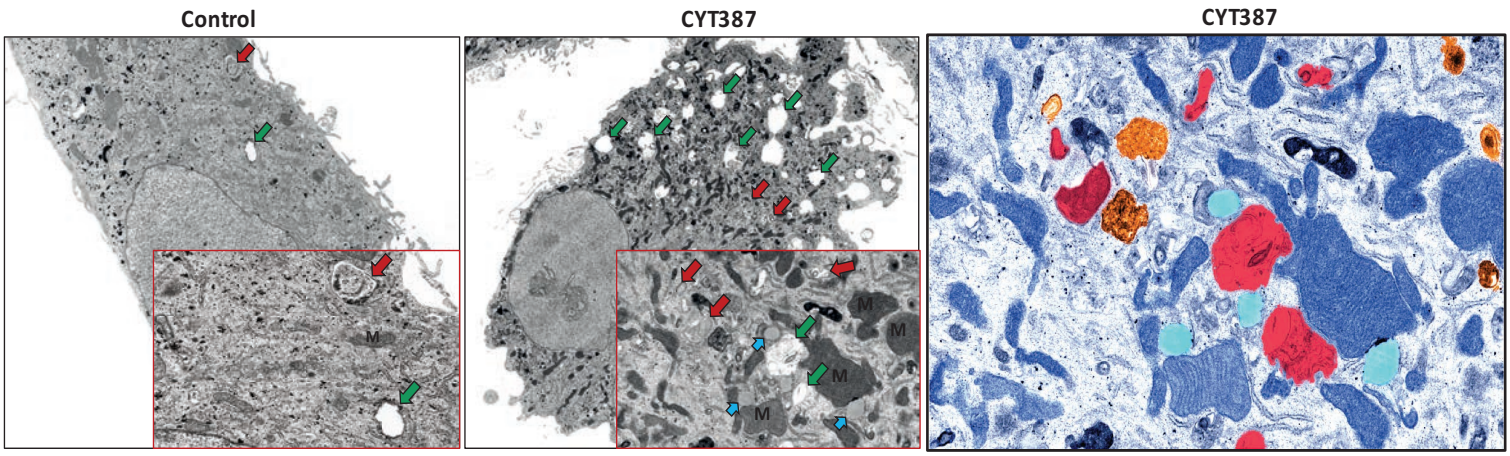

Figure 2. CYT387 combines with MK2206 to effectively inhibit PI3K-AKT-mTOR signaling in human cancer cell lines and xenografts but does not induce tumor regression

(A-B) Combination treatment with GDC0941, BX795, and MK2206 with measurement of cell viability in two human RCC cell lines, **(A)** ACHN and, (**B)** SN12C

(C-D) Same combinations as in A, I with measurement of apoptosis by cleaved-caspase 3/7 in **(C)** ACHN and, **(D)** SN12C cells.

(E-F): (E) Heatmap of signaling kinase arrays shows of effect of CYT387, MK2206 and CYT387+MK2206 co-treatment in ACHN cells at 24 hours and 72 hours after treatment. (**F)** Immunoblot for LC3, p-AKT Thr 308, p-AKT Ser 473, total AKT, p-PRAS40, total PRAS40, p-S6, total s6, p-STAT3, total STAT3 and β-actin

(G) Patient derived organotypic cultures treated with DMSO (control), CYT387, MK2206 and CYT387+MK2206 combination for 24hrs exhibit increase in LC3B (green) and decrease in p-S6 (red) and p-AKT (red).

(H) *ATG5*$^{+/+}$ and *ATG5*$^{-/-}$ murine embryonic fibroblasts (MEFs) were treated with 2μM CYT387, 10μM MK2206 and the combination for 24 hr and LC3, cleaved-caspase 3, p-AKT, p-S6, p-STAT3 and β-actin was evaluated by immunoblotting.

(I) ACHN xenografts treated with Vehicle, CYT387 (50mg/kg), MK2206 (60mg/kg) and CYT387-MK2206 (50mg/kg+60mg/kg) combination. Tumor volume is shown. Error bars represent mean ± SEM. (Con vs CYT387+MK2206 P<0.01****

(J) Effect on apoptosis (CC3) and (**K)** proliferation (KI67) in ACHN xenograft tumors. Error bars represent mean ± SEM. (**J:** Control v CYT387+MK2206 p<0.0001; **K:** Control vs CYT387+MK2206 p= 0.0018).

(L) SN12C xenografts treated with Vehicle, CYT387 (50mg/kg), MK2206 (50mg/kg) and CYT387-MK2206 (50mg/kg+60mg/kg) combination. Tumor volume is shown. Error bars represent mean ± SEM; Con vs CYT387+MK2206 p<0.0001****

(M-N): (M) Effect on apoptosis (CC3) and (**N)** proliferation (KI67) in SN12C xenograft tumors. Error bars represent mean ± SEM. (**M:** Control vs CYT387+MK2206 <0.0001; **N:** Control v CYT387+MK2206 <0.0001).

Figure 2

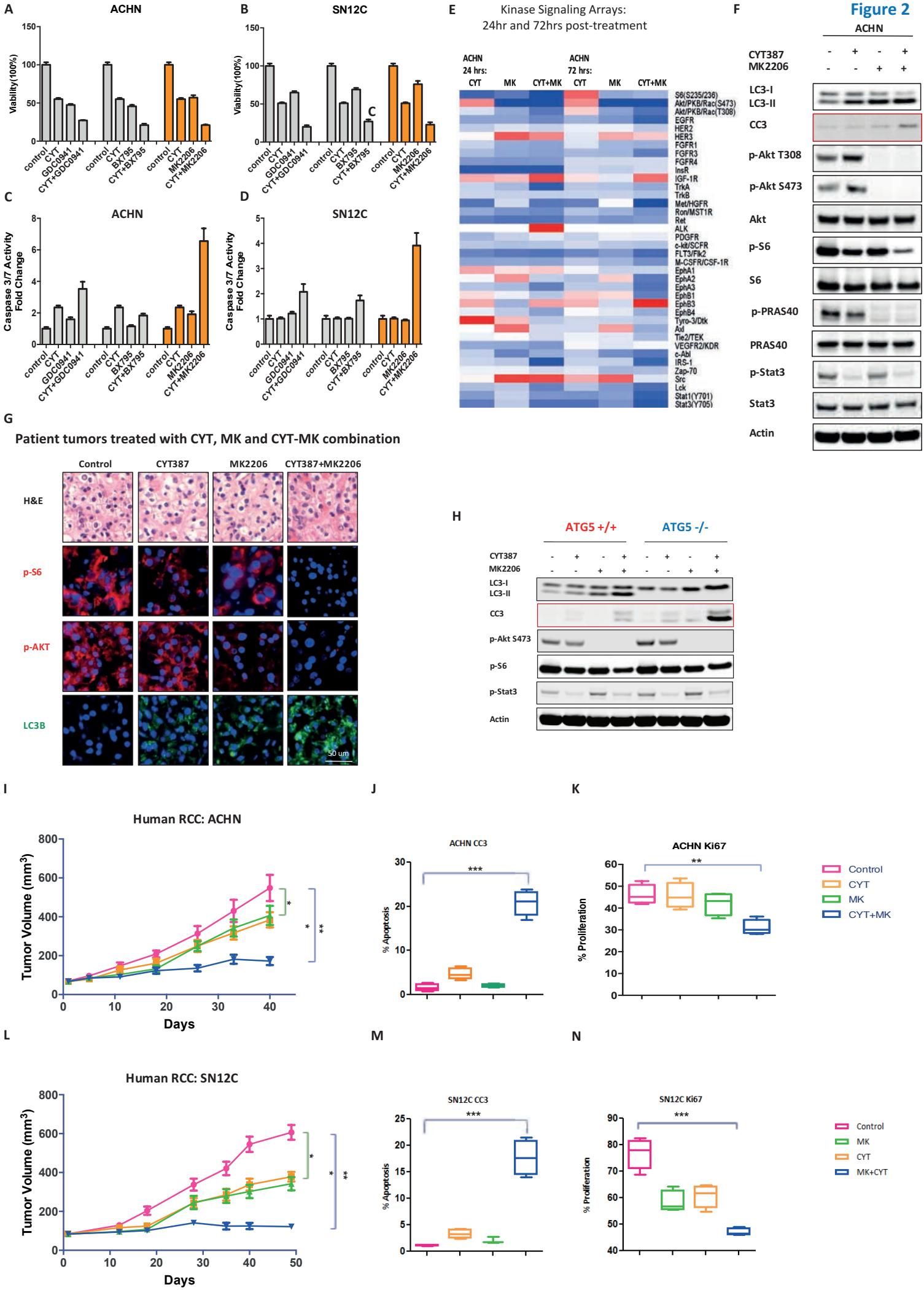
A
ACHN
Viability(100%)
control
CYT
GDC0941
CYT+GDC0941
BX795
CYT+BX795
MK2206
CYT+MK2206
B
SN12C
C
D
Caspase 3/7 Activity Fold Change
E
Kinase Signaling Arrays:
24hr and 72hrs post-treatment
ACHN 24 hrs:
ACHN 72 hrs:
CYT
MK
CYT+MK
S6(S235/236)
Akt/PKB/Rac(S473)
Akt/PKB/Rac(T308)
EGFR
HER2
HER3
FGFR1
FGFR3
FGFR4
InsR
IGF-1R
TrkA
TrkB
Met/HGFR
Ron/MST1R
Ret
ALK
PDGFR
c-kit/SCFR
FLT3/Flk2
M-CSFR/CSF-1R
EphA1
EphA2
EphA3
EphB1
EphB3
EphB4
Tyro-3/Dtk
Axl
Tie2/TEK
VEGFR2/KDR
c-Abl
IRS-1
Zap-70
Src
Lck
Stat1(Y701)
Stat3(Y705)
F
ACHN
CYT387
MK2206
LC3-I
LC3-II
CC3
p-Akt T308
p-Akt S473
Akt
p-S6
S6
p-PRAS40
PRAS40
p-Stat3
Stat3
Actin
G
Patient tumors treated with CYT, MK and CYT-MK combination
Control
CYT387
MK2206
CYT387+MK2206
H&E
p-S6
p-AKT
LC3B
50 um
H
ATG5 +/+
ATG5 -/-
CYT387
MK2206
LC3-I
LC3-II
CC3
p-Akt S473
p-S6
p-Stat3
Actin
I
Human RCC: ACHN
Tumor Volume (mm3)
Days
J
ACHN CC3
% Apoptosis
K
ACHN Ki67
% Proliferation
Control
CYT
MK
CYT+MK
L
Human RCC: SN12C
Tumor Volume (mm3)
Days
M
SN12C CC3
% Apoptosis
N
SN12C Ki67
% Proliferation
Control
MK
CYT
MK+CYT

Figure S3. CYT387-induced inhibition of mTORC1 relieves the inhibitory feedback signal transmitted from mTORC1 to PI3K with consequent hyperactivation of PI3K and AKT, Related to Figure 2

(A-B): **(A)** Heatmap of kinase arrays shows time dependent decrease in p-S6 and subsequent increase in p-AKT Ser473 and Thr308 in ACHN cells at 24 hours and 72 hours after treatment. **(B)** ACHN cells were treated with 2μM CYT387 for 5, 24 and 72 hr and lysed and probed for LC3, p-AKT Thr 308, p-AKT Ser 473, total AKT, p-S6, total s6, p-STAT3, total STAT3 and β-actin.

(C) CYT387 treatment does not activate ERK signaling. ACHN cells treated with increasing dose of CYT387 (0-3μM) and probed for LC3B, p-ERK, total ERK, p-S6 and total s6. Tubulin as loading control.

(D) Schematic of chemical dissection of PI3K-AKT-mTOR pathway with GDC-0941 (pan-PI3K inhibitor), BX-795 (PDK1 inhibitor) and MK2206 (allosteric AKT inhibitor).

(E) Combination of GDC-0941, pan-PI3K inhibitor with CYT387 in ACHN cells for 24hr. Immunoblotted with indicated antibodies.

(F) Combination of BX-795 (3μM), PDK1 inhibitor with CYT387 (2μM) in ACHN cells for 24hr. Immunoblotted with antibodies shown.

(G, H) Stable mouse weights with treatment: Vehicle, CYT387 (50mg/kg), MK2206 (60mg/kg) and CYT387-MK2206 (50mg/kg+60mg/kg) combination. Body weights of mice bearing **(G)** ACHN, and, **(H)** SN12C tumors as indicated. Data are presented as mean ± SEM; *ns*: not significant.

(I) Tumor tissue from ACHN xenografts treated with the indicated drug regimens were evaluated by immunofluorescence for p-S6 and p-AKT

Supplementary Figure 3

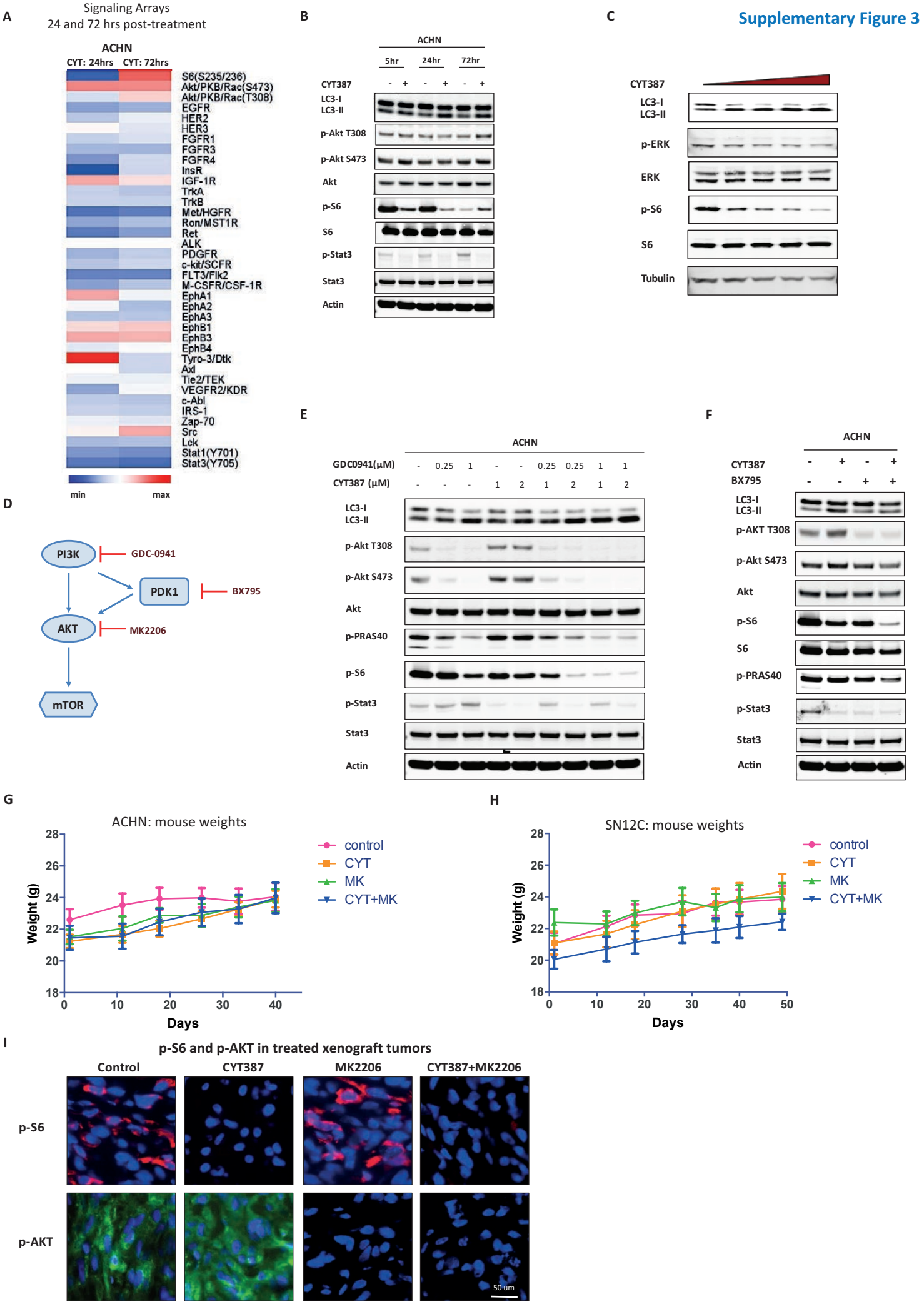

Figure 3. Effect of treatment on metabolism

(A) Treatment effect of control, CYT387, MK2206, CYT387+MK2206 on glucose uptake over time, measured by ^{18}FDG.

(B) Glucose and lactate levels in culture media were measured in control and treated cells and normalized to cell number.

(C) Qualitative analysis of cell diameter changes of ACHN cells treated with CYT387, MK2206, CYT387+MK2206 or vehicle (DMSO). (* $p<0.02$)

(D) Glycolysis in ACHN cells was measured using a XF-96 Extracellular Flux Analyzer after pre-incubation with drugs or DMSO. Shown are ECAR means ± SD of experimental triplicates.

(E) Effect of treatment on basal ECAR, measured in real time and presented as change in mpH per unit time (representative results shown, n=2)

(F) Ratios of oxygen consumption rate (OCR, indicator of OXPHSO) to extracellular acidification rates (ECAR, indicator of aerobic glycolysis at baseline) of treated ACHN cells (representative results shown, n=2)

(G-J) Treatment activates p-AMPK and increases NADPH levels, maintains GSSG/GSH ratios and mitigates ROS. ACHN cells were treated with control, 2 μM CYT387, 10 μM MK2206, CYT387+MK2206 for 24hr, and probed with the indicated antibodies **(G)**; NADP+/NADPH levels were measured **(H)**; GSSG and GSH levels were measured in lysates (n=4) (**I)** using LC-MS/MS. The normalized abundance of these metabolites is shown; Staining of cells with the ROS sensor CellRox (n=3; three independent experiments, p=ns) **(J)**.

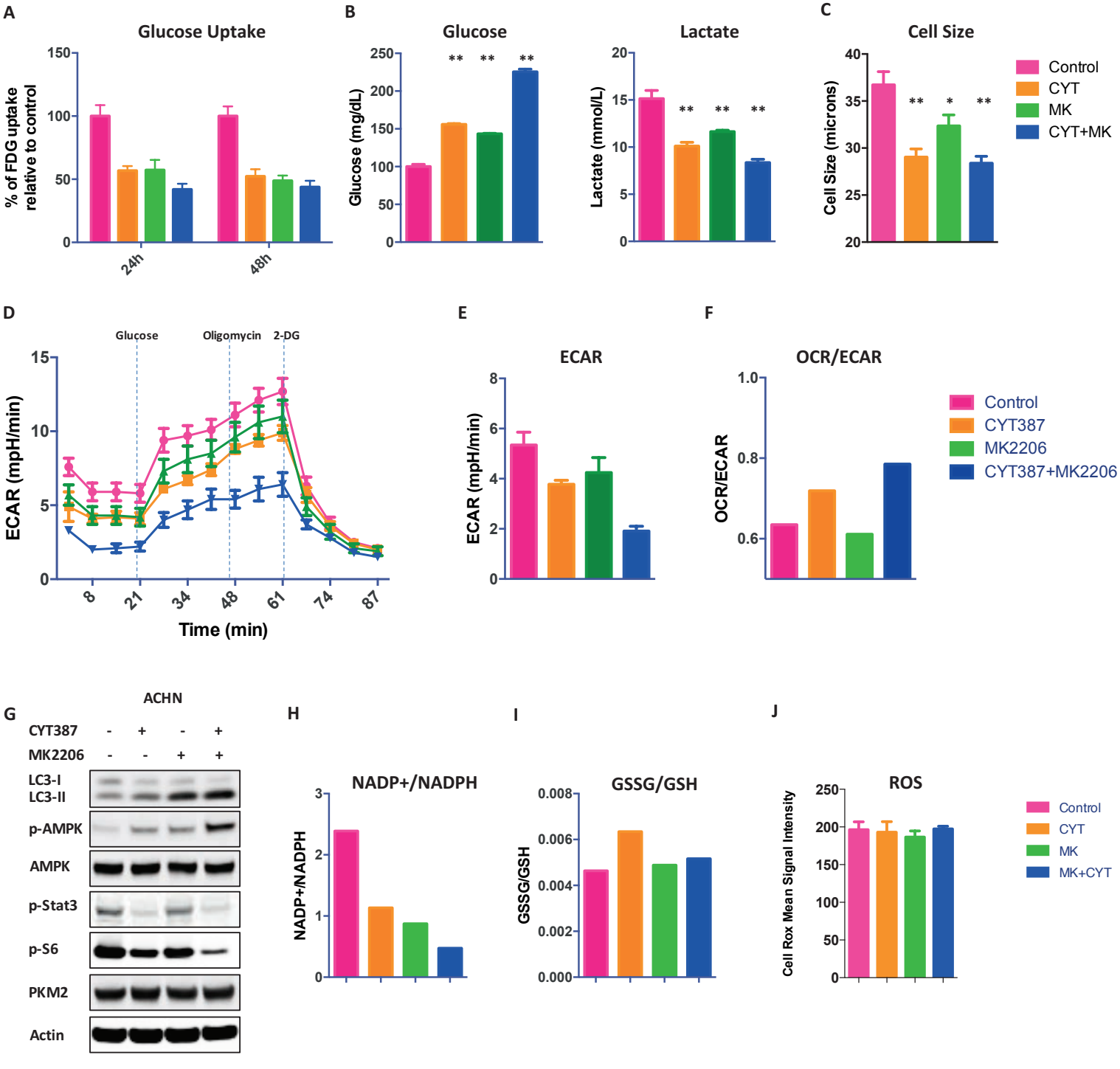
A
Glucose Uptake
% of FDG uptake relative to control
150
100
50
0
24h
48h
B
Glucose
Glucose (mg/dL)
250
200
150
100
50
0
**
**
**
Lactate
Lactate (mmol/L)
20
15
10
5
0
**
**
**
C
Cell Size
Cell Size (microns)
40
35
30
25
20
**
*
**
Control
CYT
MK
CYT+MK
D
Glucose
Oligomycin
2-DG
ECAR (mpH/min)
15
10
5
0
8
21
34
48
61
74
87
Time (min)
E
ECAR
ECAR (mpH/min)
8
6
4
2
0
F
OCR/ECAR
OCR/ECAR
1.0
0.8
0.6
Control
CYT387
MK2206
CYT387+MK2206
G
ACHN
CYT387 - + - +
MK2206 - - + +
LC3-I
LC3-II
p-AMPK
AMPK
p-Stat3
p-S6
PKM2
Actin
H
NADP+/NADPH
NADP+/NADPH
3
2
1
0
I
GSSG/GSH
GSSG/GSH
0.008
0.006
0.004
0.002
0.000
J
ROS
Cell Rox Mean Signal Intensity
250
200
150
100
50
0
Control
CYT
MK
MK+CYT

Figure 4. PI3K-AKT-mTOR signaling inhibition induces metabolic reprogramming

(A) Heatmap of metabolomic profiling of treated cells (CYT387, MKK2206, CYT+MMK2206) compared to ACHN cells treated with vehicle (DMSO) using LC-MS/MS (see methods for details). Log fold changes of profiled metabolites are shown; metabolites are ordered within each category; Glycolysis, tricarboxylic acid cycle (TCA), pentose phosphate pathway (PPP), nucleotide metabolism, amino acid metabolism, phospholipids, ether phospholipids, lysophospholipids, fatty acids, neutral lipids, acyl carnithines (AC), sphingolipids (SL), n-acyl ethanolamines (NAE).

(B) Phospholipase A2 catalyzes the hydrolysis of phospholipids to lysophospholipids and arachidonic acid. Waterfall plot demonstrating relative levels of phospholipids, lysophospholipids, and fatty acids in treated cells (CYT387, MK2206, CYT+MK2206) compared to ACHN cells treated with vehicle (DMSO). Stars denote a significant difference of treated cells compared to vehicle (t-test p-value ≤ 0.05).

A

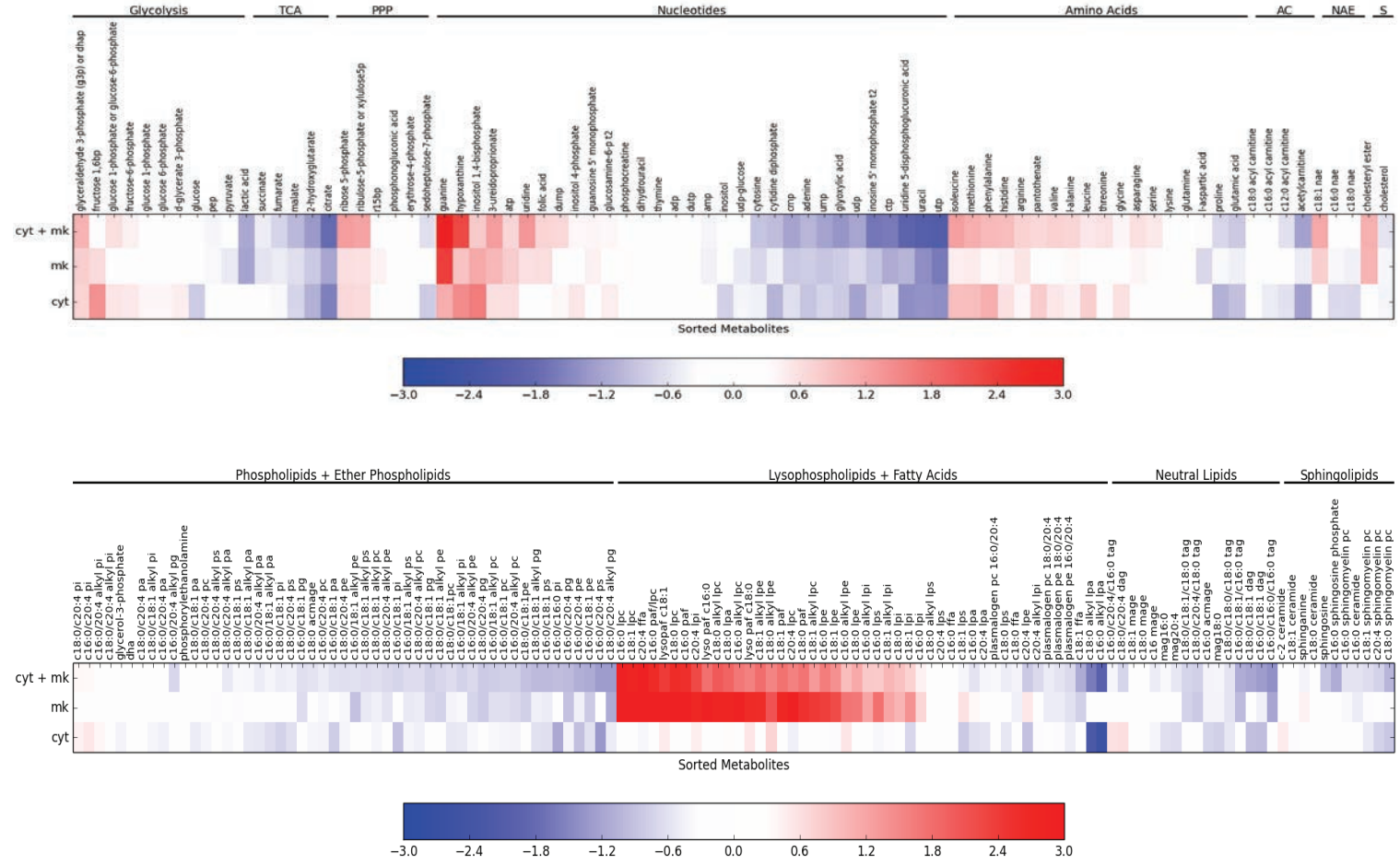
Metabolic Profiling
Glycolysis
TCA
PPP
Nucleotides
Amino Acids
AC
NAE
S
cyt + mk
mk
cyt
Sorted Metabolites
−3.0
−2.4
−1.8
−1.2
−0.6
0.0
0.6
1.2
1.8
2.4
3.0

Phospholipids + Ether Phospholipids
Lysophospholipids + Fatty Acids
Neutral Lipids
Sphingolipids
cyt + mk
mk
cyt
Sorted Metabolites
−3.0
−2.4
−1.8
−1.2
−0.6
0.0
0.6
1.2
1.8
2.4
3.0

B

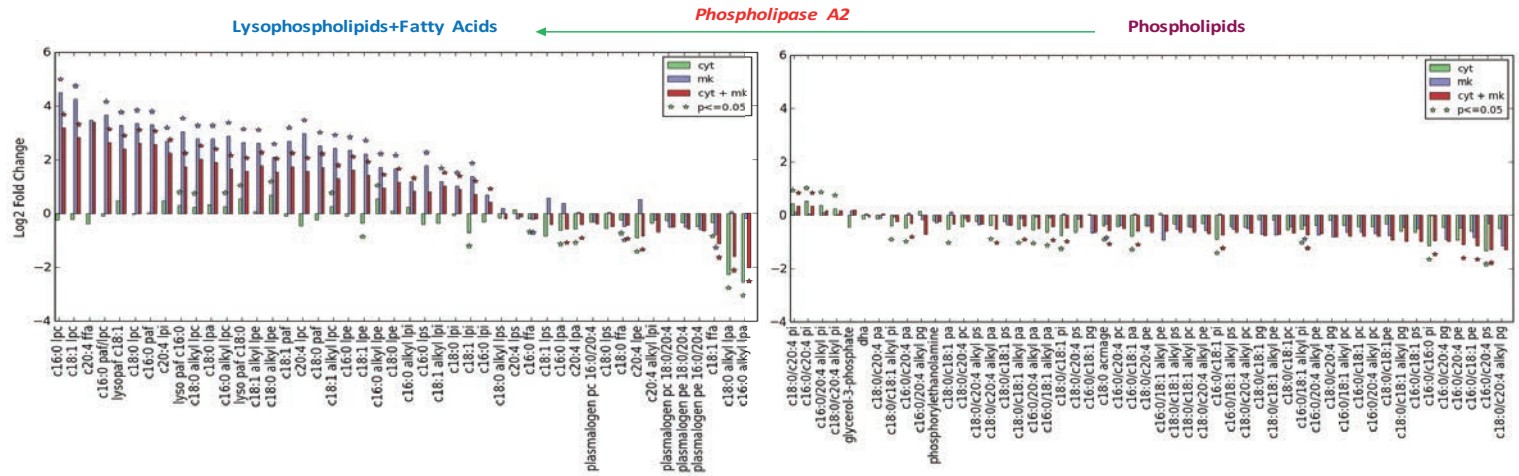
Lysophospholipids+Fatty Acids
Phospholipase A2
Phospholipids
Log2 Fold Change
cyt
mk
cyt + mk
p<=0.05

Figure S4. Metabolic changes in vehicle treated compared to CYT387, MK2206 and CYT387+MK2206 treatment, Related to Figure 4

(A-F) Metabolic pathway alterations in treated cells (CYT387, MK2206, CYT387+MK2206) compared to ACHN cells treated with vehicle (DMSO. Log fold change abundance of metabolites in glycolysis, pentose phosphate pathway, TCA cycle, amino acid, nucleotide biogenesis and neutral lipids are shown. Stars denote a significant difference of treated cells compared to vehicle (t-test p-value ≤ 0.05).

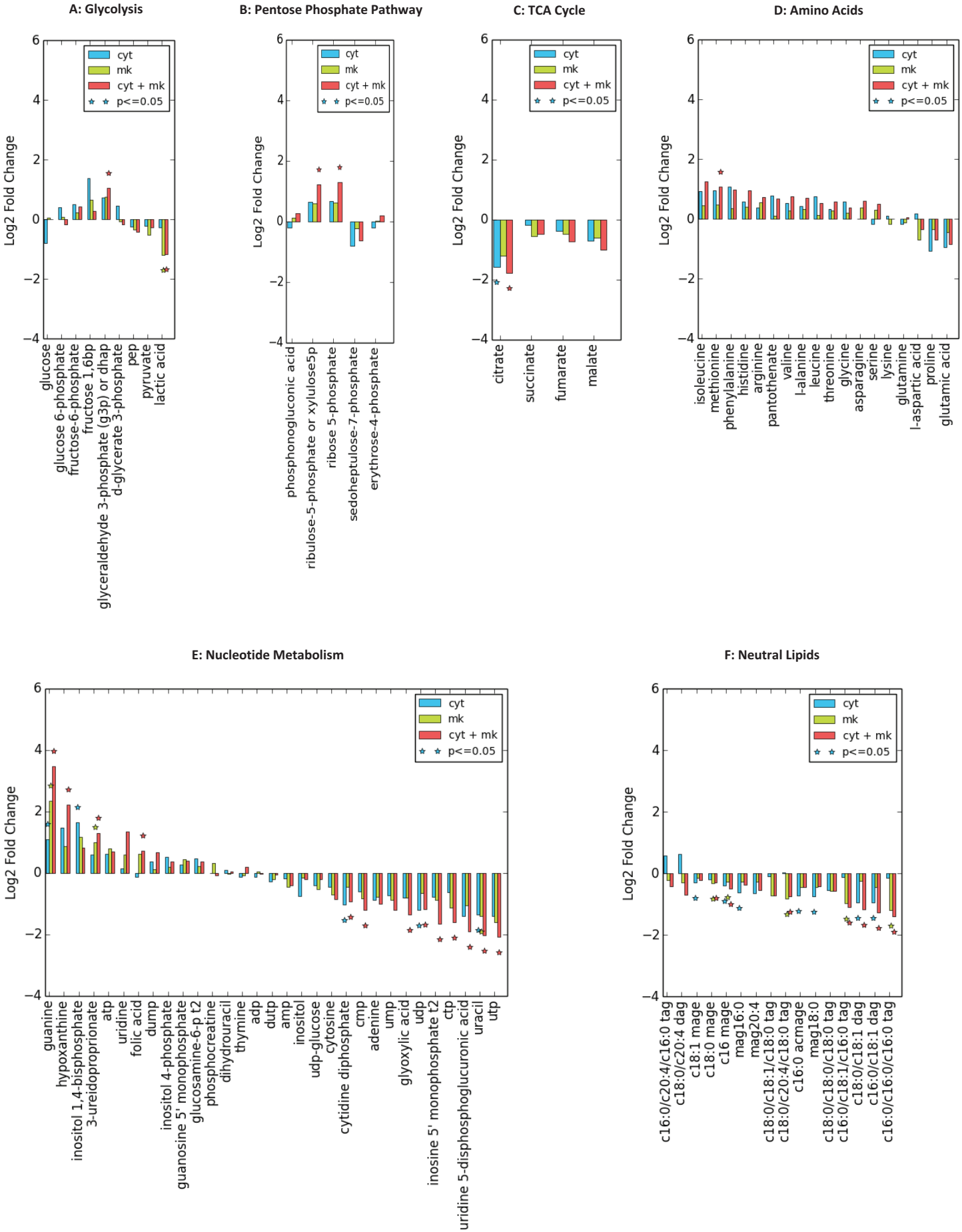
A: Glycolysis
B: Pentose Phosphate Pathway
C: TCA Cycle
D: Amino Acids
E: Nucleotide Metabolism
F: Neutral Lipids
cyt
mk
cyt + mk
p<=0.05
Log2 Fold Change
glucose
glucose 6-phosphate
fructose-6-phosphate
fructose 1,6bp
glyceraldehyde 3-phosphate (g3p) or dhap
d-glycerate 3-phosphate
pep
pyruvate
lactic acid
phosphonogluconic acid
ribulose-5-phosphate or xylulose5p
ribose 5-phosphate
sedoheptulose-7-phosphate
erythrose-4-phosphate
citrate
succinate
fumarate
malate
isoleucine
methionine
phenylalanine
histidine
arginine
pantothenate
valine
l-alanine
leucine
threonine
glycine
asparagine
serine
lysine
glutamine
l-aspartic acid
proline
glutamic acid
guanine
hypoxanthine
inositol 1,4-bisphosphate
3-ureidoproprionate
atp
uridine
folic acid
dump
inositol 4-phosphate
guanosine 5' monophosphate
glucosamine-6-p t2
phosphocreatine
dihydrouracil
thymine
adp
dutp
amp
inositol
udp-glucose
cytosine
cytidine diphosphate
cmp
adenine
ump
glyoxylic acid
udp
inosine 5' monophosphate t2
ctp
uridine 5-disphosphoglucuronic acid
uracil
utp
c16:0/c20:4/c16:0 tag
c18:0/c20:4 dag
c18:1 mage
c18:0 mage
c16 mage
mag16:0
mag20:4
c18:0/c18:1/c18:0 tag
c18:0/c20:4/c18:0 tag
c16:0 acmage
mag18:0
c18:0/c18:0/c18:0 tag
c16:0/c18:1/c16:0 tag
c18:0/c18:1 dag
c16:0/c18:1 dag
c16:0/c16:0/c16:0 tag

Figure S5. Generation of bioactive eicosanoids from arachidonic acid, Related to Figure 4

(A) Schematic of biosynthesis of eicosanoids from arachidonic acid.

(**B)** Levels of P450-derived and Arachidonic Acid-derived metabolites in ACHN human RCC cells treated with the MK2206-CYT387 combination

Supplementary Figure 5

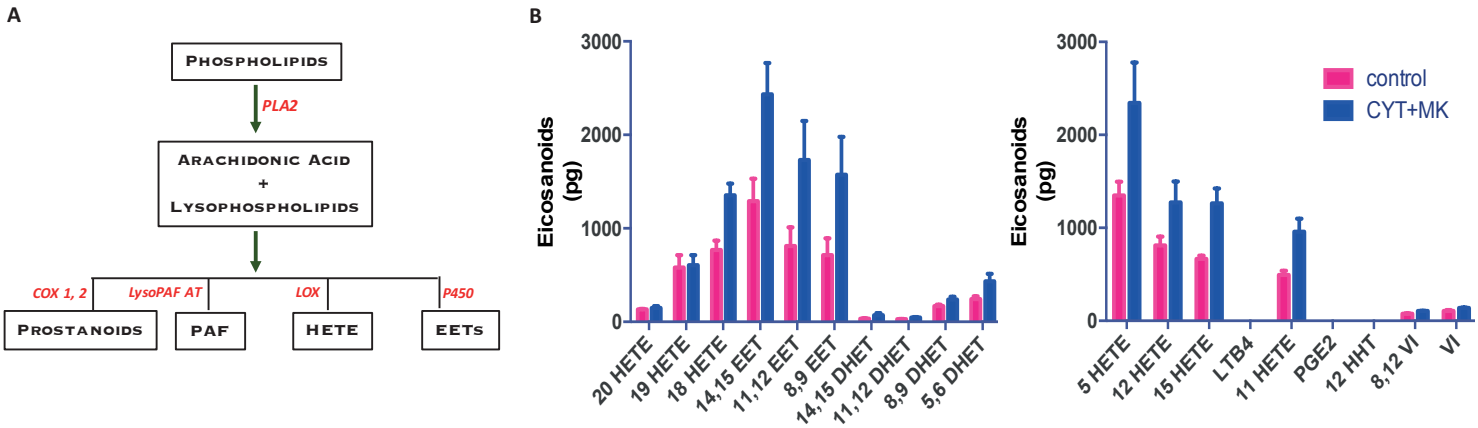

Figure 5. Autophagy is required for lipid droplet growth and fatty acid oxidation

(A) ACHN cells were treated with control, CYT387, MK2206, CYT387+MK2206 for 24hrs, Bodipy 493/503 (green) was added to visualize lipid droplets. Representative images shown (n=5 experiments).

(B-C) Bar graphs quantify the increase in **(B)** number and, **(C)** size of lipid droplets, respectively. Data are expressed as means ±SEM. *p<.001 for Control v CYT387, control v MK2206, control v CYT387+MK2206

(D) Adipophilin staining in xenograft tumors quantifies increase in LDs *in vivo* (n=9). Data are expressed as means ±SEM, *p<.01, control v CYT387, control v MK2206, **p<.001 control v CYT387+MK2206. Measured in tumors resected after 40 days of treatment.

(E) *ATG5* $^{+/+}$ murine embryonic fibroblasts were treated with 2μM CYT387, 10μM MK2206 and the combination for 24 hr. Bodipy was added and the lipid droplet number was measured. n=500 cells, *p<.001 control v CYT387, control vs CYT387+MK2206, p<.005 for control v MK2206.

(F) *ATG5* $^{-/-}$ murine embryonic fibroblasts treated as in G. Bodipy was added and the lipid droplet number was measured. n=500 cells, p=NS: no significance between treatment groups.

(G) *ATG5 +/+* and *ATG5 -/-* murine embryonic fibroblasts were treated with DMSO (control), CYT387, MK2206, CYT387+MK2206, for 24 h and then oxygen consumption rates (OCR, indicator of OXPHOS) was determined using a XF-96 Extracellular Flux Analyzer during sequential treatments (dotted vertical lines) with oligomycin, FCCP, and rotenone/antimycin (A+R), Spare respiratory capacity SRC: the quantitative difference between maximal uncontrolled OCR (top horizontal dashed line) and the initial basal OCR (bottom horizontal dashed line). Shown are OCR means ± SD of experimental triplicates. For ease of viewing, only control, CYT387+MK2206 data is graphed.

(H) Spare Respiratory Capacity (SRC) (% max OCR after FCCP injection of baseline OCR) of ATG5 +/+ and -/- murine embryonic fibroblasts after indicated treatment. Shown are means ± SD of experimental triplicates.

(I) Ratios of oxygen consumption rate (OCR) to extracellular acidification rates (ECAR, indicator of aerobic glycolysis) at baseline of ATG5 +/+ and ATG5 -/- murine embryonic fibroblasts after indicated treatment.

(J) ACHN cells were treated with control, CYT387, MK2206, CYT387+MK2206 for 24hrs, Mitotracker Orange was added to visualize mitochondria. Representative images shown (n=5 experiments). Mitochondria number was measured, and data is expressed as means ±SEM. *p<.001 control v CYT, control v MK, control vs MK+CYT

(K) Dual staining of Bodipy and Mitotracker Orange demonstrate close proximity of lipid droplets with mitochondria in CYT387+MK2206 co-treated ACHN cells (representative image shown)

(L) Global metabolite profiling reveals a preferential decrease in lipids. Decrease: abundance less than 0.5-fold in treated cells compared to the vehicle. Increase: abundance greater than 2-fold in treated cells compared to the vehicle.

(M) Fatty acid fuel dependency measures the reliance of ACHN cells on fatty acids to maintain baseline respiration. ACHN cells were treated with DMSO (control), CYT387+MK2206, for 24 h and OCR was measured during the Seahorse XF Mito Fuel Flex assay. The percent dependence on fatty acids was calculated by quantifying the change in basal OCR after fatty acid oxidation was blocked using the CPT-1a inhibitor, Etomoxir (4 μM) divided by the total change in OCR from baseline after combined inhibition of fatty acid, glutamine and pyruvate oxidation using 4 μM Etomoxir, 3 μM BPTES and 2 μM UK5099, respectively (representative graph, n=2). Fatty acid fuel flexibility is calculated by measuring the change in sensitivity to Etomoxir's inhibition of OCR after blockade of glutamine and glucose oxidation, and represents the ability of ACHN cells to increase oxidation of fatty acid when glutamine and pyruvate utilization is precluded.

(N) Measurement of fatty acid driven OCR, measured by acute inhibition of CPT-1a using 4 μM Etomoxir (*$p<0.01$) and represented as a percentage of total mitochondria OCR calculated using mitochondrial complex I and III inhibitors, 1 μM Rotenone and 1 μM Antimycin, respectively.

Lipid Droplets (LD)

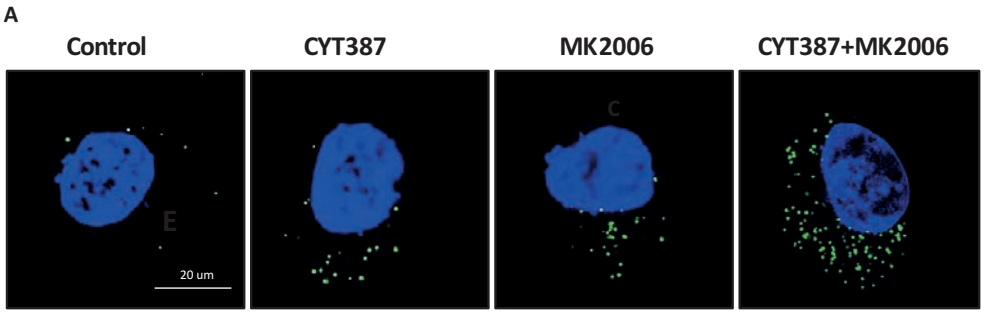

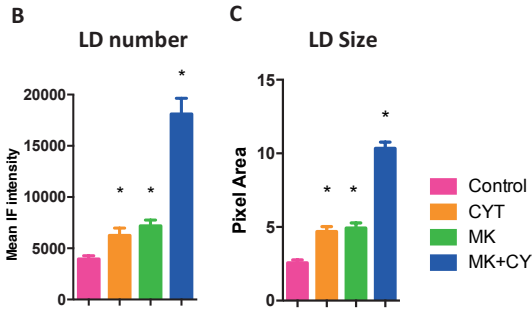

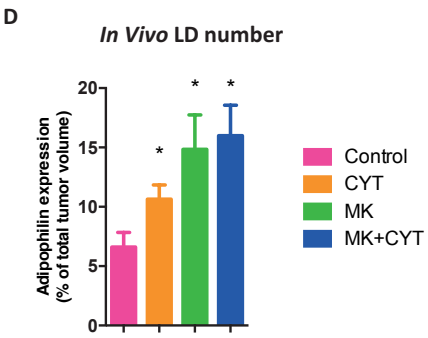

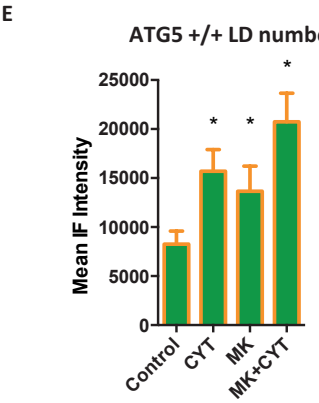

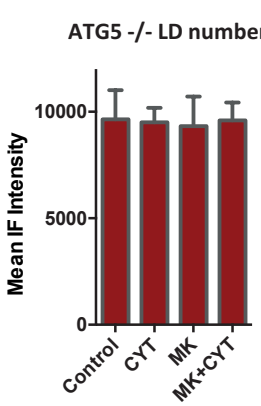

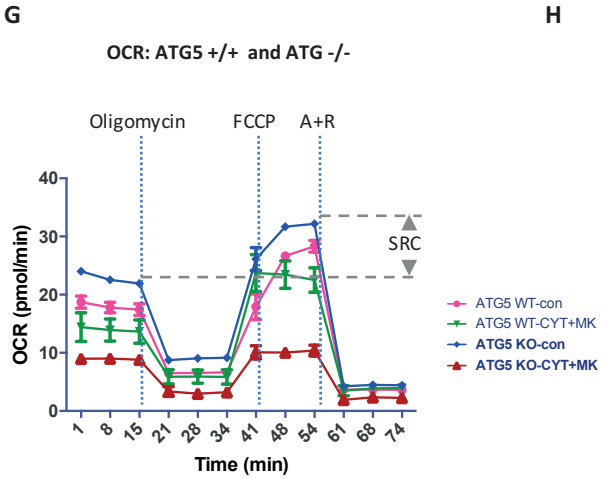

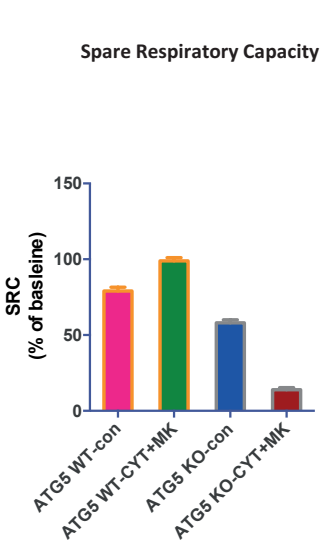

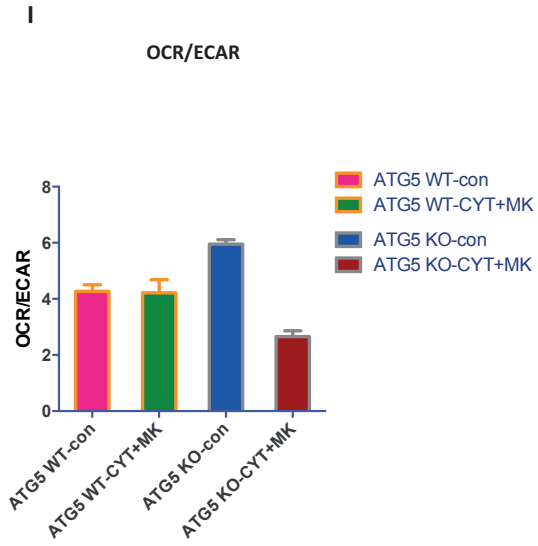

Mitochondria

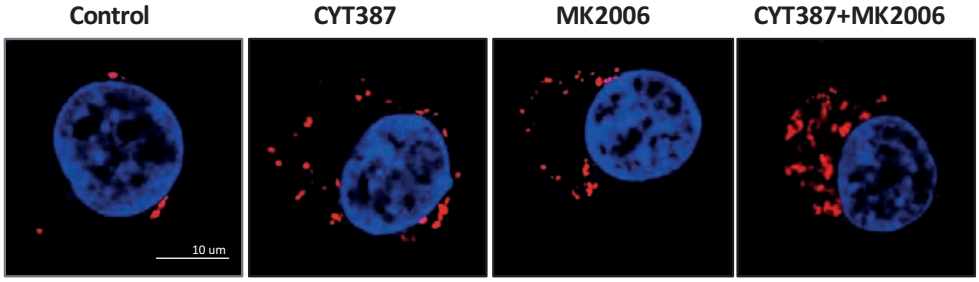

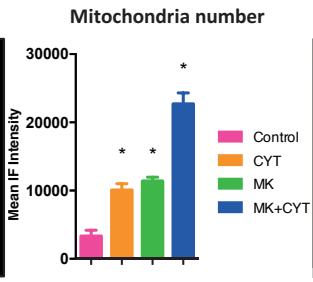

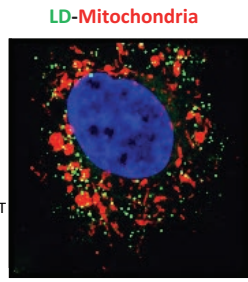

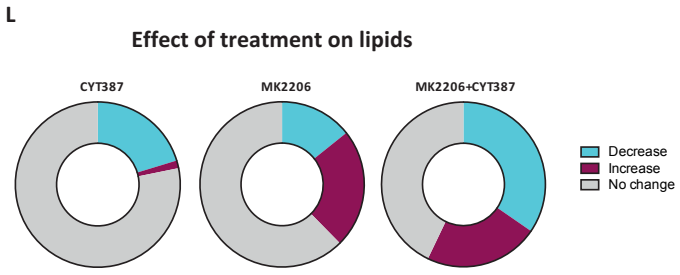

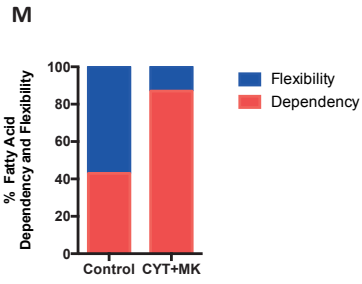

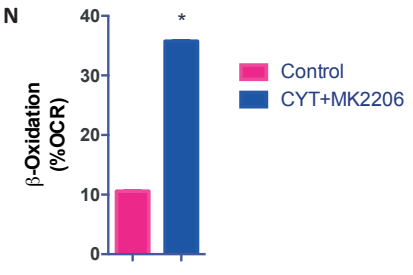

Figure S6. Phospholipid derived fatty acid incorporation into lipid droplets is induced by CYT387-MK2206 co-treatment in ACHN, Related to Figure 5

ACHN incubated with BODIPY-C12-HPC, a phospholipid containing a green fluorescent long chain fatty acid, for 16hrs with and without CYT387-MK2206 co-treatment. CYT387-MK2206 co-treatment led to a greater degree of incorporation of BODIPY-fatty acids into lipid droplets relative to vehicle ACHN, indicating CYT387-MK2206 co-treatment leads to an induction in phospholipid derived fatty acid to lipid droplet incorporation.
Left panel: Control (vehicle); **Right panel:** CYT387+MK2206.
Green: Bodipy-C12-HPC; Purple: wheat germ agglutinin to mark cell membrane

Supplementary Figure 6

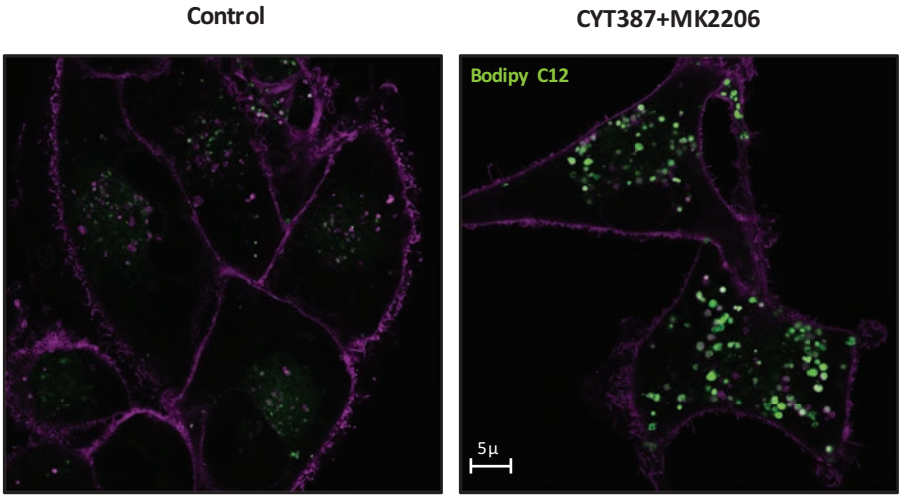

Figure S7. Comparison of fatty acid driven OCR induction by CYT387+MK2206 treatment in *ATG5* +/+ and *ATG5* -/- MEFs, Related to Figure 5.

Fatty acid driven OCR was calculated as previously described (see Figure 5N) using the CPT-1a inhibitor, etomoxir, and normalized to the total mitochondrial OCR using Antimycin and Rotenone. The percent increase in fatty acid driven OCR in ATG5 +/+ and ATG5 -/- by CYT387+MK2206 treatment is shown (n=2).

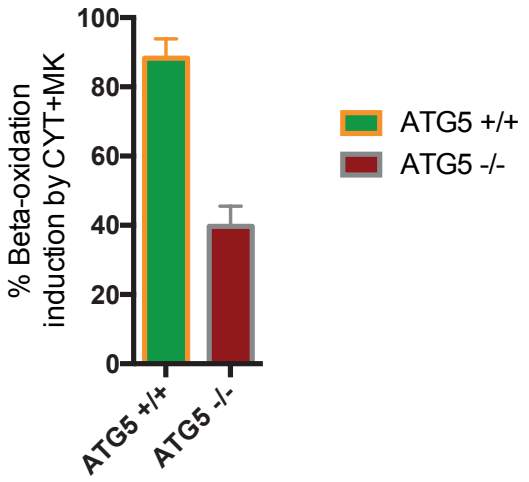
% Beta-oxidation induction by CYT+MK
100
80
60
40
20
0
ATG5 +/+
ATG5 -/-
ATG5 +/+
ATG5 -/-

Figure S8. Glutamine fuel dependency as measured using the Seahorse XF Mito Fuel Flex assay, Related to Figure 5.

ACHN cells were treated with DMSO (control), CYT387+MK2206, for 24 h and OCR was measured before and after injection of glutaminase inhibitor BPTES (3 μM). The change in basal OCR after BPTES injection was normalized to the total change in OCR after inhibition of fatty acid oxidation, glutamine and pyruvate oxidation using Etomoxir, BPTES and UK5099, respectively (representative graph, n=2). The ability of ACHN cells to upregulate glutamine OCR, flexibility, is calculated by measuring the change in sensitivity to BPTES inhibition of OCR after blocking fatty acid and pyruvate oxidation.

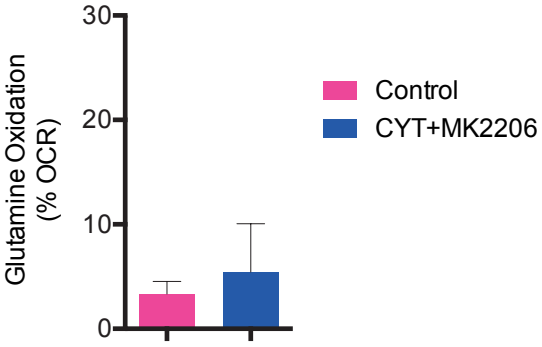
Glutamine Oxidation
(% OCR)
30
20
10
0
Control
CYT+MK2206

Figure 6: Hydrolysis of phospholipid supplies lysophospholipids and fatty acids for cancer cell survival

A: ACHN cells were treated with control, OOEPC, CYT387, CYT387+OOEPC, MK2206, MK2206+OOEPC, CYT387+MK2206, CYT387+MK2206+OOEPC for 24hrs, Bodipy 493/503 (green) was added to visualize lipid droplets. Representative images shown (n=3 experiments)

B: Bar graphs quantify the number of lipid droplets. Data are expressed as means ±SEM. *p<.0001 CYT387 v CYT387 +OOEPC, MK2206 v MK2206+OOEPC, CYT387+MK2206 v CYT387+MK2206+OOEPC

C, D: ACHN cells were treated with DMSO (control), OOEPC, CYT387, CYT387+OOEPC, MK2206, MK2206+OOEPC, CYT387+MK2206, CYT387+MK2206+OOEPC for 24 h and then oxygen consumption rates (OCR) was determined using a XF-96 Extracellular Flux Analyzer during sequential treatments with oligomycin, FCCP, and rotenone/antimycin (A+R); **D:** Initial basal OCR, maximal OCR, Spare respiratory capacity (SRC: the quantitative difference between maximal uncontrolled OCR and the initial basal OCR), and ATP production is depicted in the plot. Shown are OCR means ± SD of experimental triplicates. For ease of viewing, only control, OOEPC, CYT387+MK2206, CYT387+MK2206+OOEPC data is graphed.

E: OCR versus ECAR (means ±SEM, experimental triplicates) after the addition of OOEPC to the CYT387-MK2206 combination (Con: Control; O: OOEPC; C+M: CYT387+MK2206; C+M+O: CYT387+MK2206+OOEPC)

F, G: Cell viability **(F)** and Caspase3/7 activity **(G)** with addition of OOEPC to CYT387, MK2206, CYT387+MK2206 (n=3). Data are expressed as means ±SD. (**G:** CYT387+MK2206 vs CYT387+MK2206+OOEPC: p=ns**; H:** CYT387+MK2206 vs CYT387+MK2206+OOEPC: p<0.001, ***)
H: The effect of adding Varespladib, a distinct PLA2 inhibitor to CYT387, MK2206, CYT387+MK2206 on lipid droplet numbers was evaluated with Bodipy staining

I, J: Cell viability **(I)** and Caspase3/7 activity **(J)** with addition of Varespladib, a distinct PLA2 inhibitor to CYT387, MK2206, CYT387+MK2206 (n=3). Data are expressed as means ±SD. (**I:** CYT387+MK2206 vs CYT387+MK2206+Varespladib: p<0.01, **; **J:** CYT387+MK2206 vs CYT387+MK2206+Varespladib: p<0.1, *)

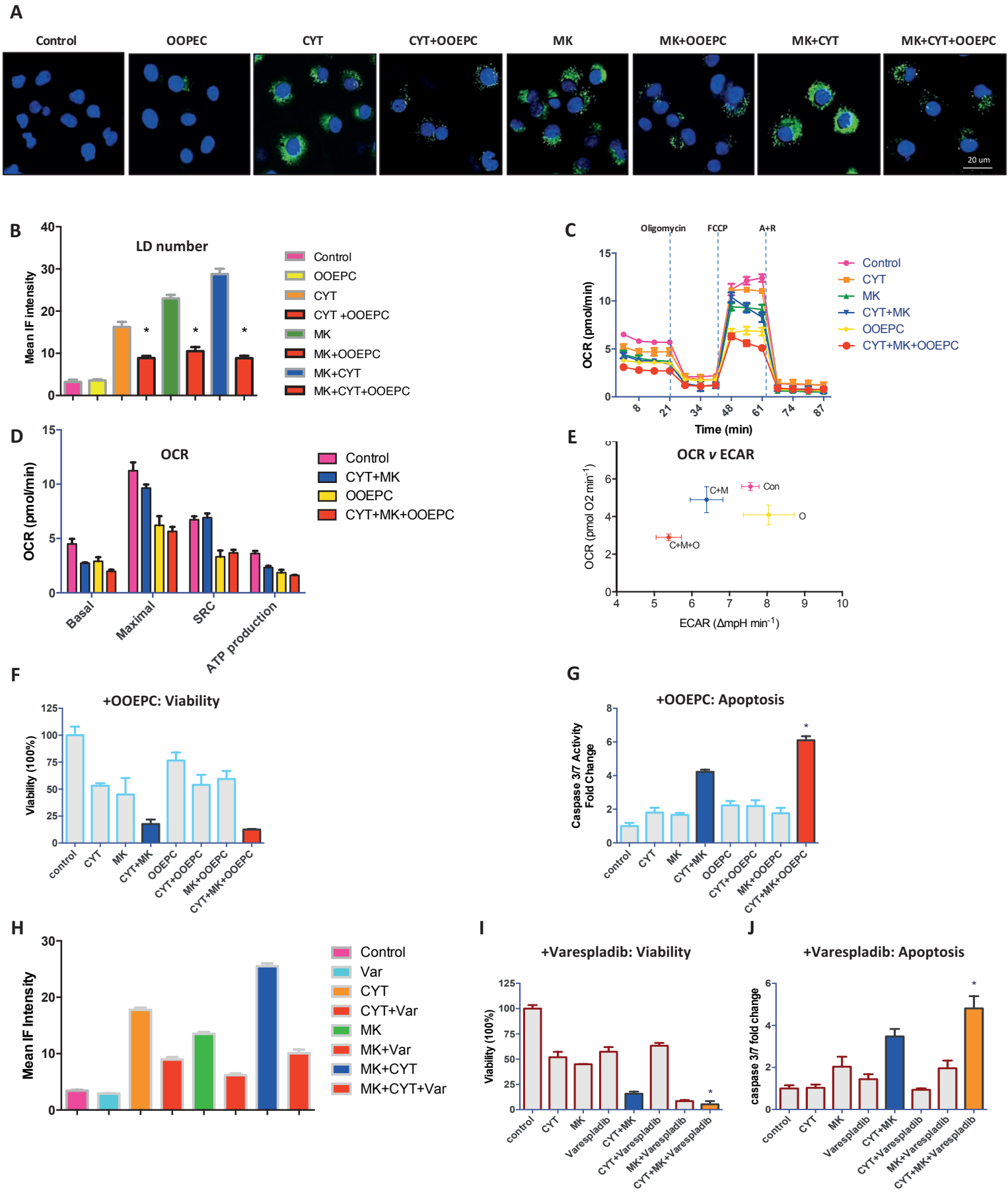
A
Control
OOPEC
CYT
CYT+OOEPC
MK
MK+OOEPC
MK+CYT
MK+CYT+OOEPC
20 um
B
LD number
Mean IF intensity
Control
OOEPC
CYT
CYT +OOEPC
MK
MK+OOEPC
MK+CYT
MK+CYT+OOEPC
C
Oligomycin
FCCP
A+R
OCR (pmol/min)
Time (min)
Control
CYT
MK
CYT+MK
OOEPC
CYT+MK+OOEPC
D
OCR
OCR (pmol/min)
Control
CYT+MK
OOEPC
CYT+MK+OOEPC
Basal
Maximal
SRC
ATP production
E
OCR v ECAR
OCR (pmol O2 min-1)
ECAR (ΔmpH min-1)
C+M
Con
O
C+M+O
F
+OOEPC: Viability
Viability (100%)
control
CYT
MK
CYT+MK
OOEPC
CYT+OOEPC
MK+OOEPC
CYT+MK+OOEPC
G
+OOEPC: Apoptosis
Caspase 3/7 Activity Fold Change
H
Mean IF Intensity
Control
Var
CYT
CYT+Var
MK
MK+Var
MK+CYT
MK+CYT+Var
I
+Varespladib: Viability
Viability (100%)
control
CYT
MK
Varespladib
CYT+MK
CYT+Varespladib
MK+Varespladib
CYT+MK+Varespladib
J
+Varespladib: Apoptosis
caspase 3/7 fold change

Figure S9. Effect of inhibiting different PLA2 isoforms on lipid droplet number, Related to Figure 6

ACHN cells were treated with control, inhibitors; for calcium-sensitive PLA2 (cPLA2; cPLA2i), calcium-insensitive PLA2 (iPLA2; bromoenol lactone: BEL), CYT387+MK2206, CYT387+MK2206+cPLA2i, CYT387+MK2206+BEL for 24hrs, Bodipy 493/503 was added to visualize lipid droplets (n=2 experiments). Data are expressed as means ±SEM. *p=0.0065 CYT387+MK v CYT387+MK2206 +BEL; p=0.01 CYT387+MK2206 v CYT387+MK2206+cPLA2i

Supplementary Figure 9

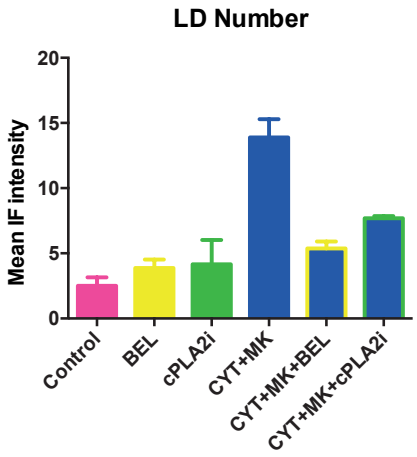

Figure S10. PLA2 inhibition by OOPEC blocks the generation of lipid droplets, Related to Figure 6

ACHN cells were treated with control, OOEPC, CYT387+MK2206, CYT387+MK2206+OOEPC added after 2hrs, CYT387+MK2206+OOEPC added after 2hrs+Etomoxir added after 8hrs, and monitored for 24hrs, Bodipy 493/503 (green) was added to visualize lipid droplets.
Data are expressed as means ±SEM (n=2). p<.0001 OOPEC v CYT387+MK2206, OOEPC added at 2hrs v CYT387+MK2206, OOPEC added at 2hrs v CYT387+MK2206+OOEPC added at 2hrs+Etomoxir added at 8hrs.
Right panel: Bar graph with all conditions, for ease of viewing, all controls are in grey; **Left panel:** Line graph of CYT+MK+OOEPC added after 2hrs compared to CYT+MK+ OOEPC added after 2hrs+Etomoxir added after 8hrs.

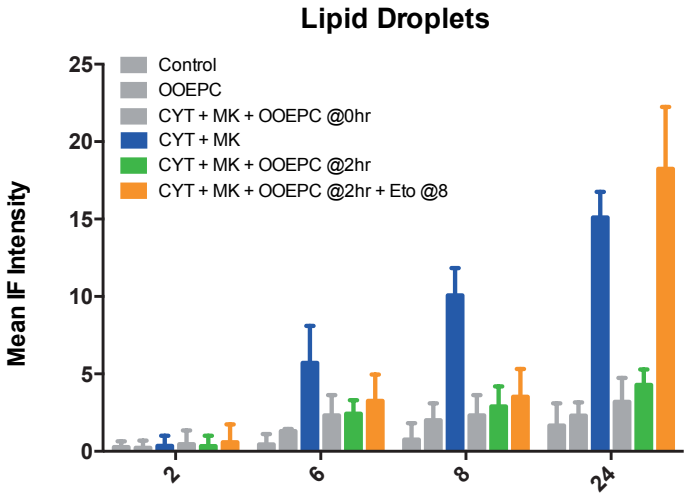
Lipid Droplets
Mean IF Intensity
25
20
15
10
5
0
Control
OOEPC
CYT + MK + OOEPC @0hr
CYT + MK
CYT + MK + OOEPC @2hr
CYT + MK + OOEPC @2hr + Eto @8
2
6
8
24

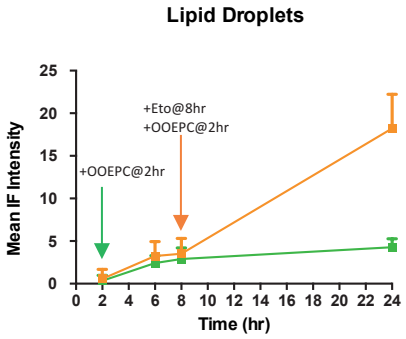
Lipid Droplets
Mean IF Intensity
25
20
15
10
5
0
+Eto@8hr
+OOEPC@2hr
+OOEPC@2hr
0 2 4 6 8 10 12 14 16 18 20 22 24
Time (hr)

Supplementary Tables:

S1: Small Molecule Inhibitor library

S2-9: Phosphoproteomics Screen

S10-11: DAVID Analysis

S12: GSEA analysis across multiple datasets show enrichment for metabolic processes

S13: RNA Seq of CYT-treated ACHN cells, related to Table S12

S14: Metabolomics Profiling

A

Gene Set Enrichment Analysis: Upregulated by CYT387 treatment

NAME	ES	NES	NOM p-val	FDR q-val
KEGG_LYSOSOME	0.2757418	1.884291	0.006134969	0.0972510
KEGG_PEROXISOME	0.3102181	1.8753588	0.007360673	0.0935007
KEGG_ARACHIDONIC_ACID_METABOLISM	0.4300354	1.7937591	0.02093596	0.1290122
KEGG_PPAR_SIGNALING_PATHWAY	0.3400262	1.6798229	0.04659091	0.1694463
REACTOME_GLYCOSPHINGOLIPID_METABOLISM	0.4430197	2.1256926	0.005740528	0.1784709
REACTOME_SPHINGOLIPID_METABOLISM	0.3254659	1.8902652	0.007616975	0.0982842
REACTOME_PEROXISOMAL_LIPID_METABOLISM	0.4448048	1.8385218	0.013853904	0.1099082
BIOCARTA_PGC1A_PATHWAY	0.4390134	1.8958447	0.010909091	0.7568732
PERERA_AUTOPHAGY (PMID: 26168401)	0.2947966	2.0634909	0.006066734	0.0060667
CARMADA_FATTY ACID METABOLISM (PMID: 26950360)	0.2739853	2.029036	0.017034069	0.0170340
GARCIA-CAO_PGC1A (PMID: 22408183)	0.4279453	1.731552	0.020125786	0.0201257

B

Gene Set Enrichment Analysis: Downregulated by CYT387 treatment

NAME	ES	NES	NOM p-val	FDR q-val
KEGG_PYRIMIDINE_METABOLISM	-0.27513558	-3.2543876	0	0
REACTOME_CELL_CYCLE	-0.26058355			1
REACTOME_CELL_CYCLE_MITOTIC	-0.30004632			1
REACTOME_METABOLISM OF_PROTEINS	-0.089255795			1
REACTOME_METABOLISM OF_RNA	-0.328743			1
REACTOME_SYNTHESIS_OF DNA	-0.48222235	-6.12676	0	0
REACTOME_S_PHASE	-0.42046085	-5.4615655	0	0
REACTOME_G1_S_TRANSITION	-0.38706166	-5.0486703	0	0